INTERNATIONAL ATOMIC ENERGY AGENCY
UNITED NATIONS EDUCATIONAL, SCIENTIFIC AND CULTURAL ORGANIZATION
INTERNATIONAL CENTRE FOR THEORETICAL PHYSICS
I.C.T.P., P.O. BOX 586, 34100 TRIESTE, ITALY, CABLE: CENTRATOM TRIESTE

H4-SMR 471/19

COLLEGE ON MEDICAL PHYSICS

10 - 28 SEPTEMBER 1990

NMR IMAGING

Lynn W. Jelinski

AT & T Bell Laboratories
Murry Hill, NJ
USA

L. W. Jelinski "in" Nuclear Magnetic Resonance Spectroscopy" by F.A. Bovey, 2nd Ed., Academic Press, 1988. pages 489 - 505.

sign. Three-bond couplings, $^{1}P-O-C-^{1}H$, show the expected Karplus-like angular dependence, the coupling being of the order of 20 Hz when ϕ is *ca.* 180°. This relationship in $^{31}P-O-C-^{1}H$ and, $^{31}P-O-C-^{13}C$, fragments has been used to determine the conformation about the ribose-phosphate backbone of nucleotides and nucleic acids in solution.

^{31}P NMR spectroscopy has become of great importance not only in the study of polynucleotide structure but also in the observation of metabolic processes *in vitro* and *in vivo*. In Fig. 9.4 is shown the 73.8 MHz ^{31}P spectrum of adenosine triphosphate (ATP) in aqueous solution at pH 7.0[43]: The splitting of the α, β, and γ phosphorus resonances arises from the ^{31}P-^{31}P couplings (tabulated in Table 9.4). It is possible to observe this and other phosphorus-containing metabolites *in vivo* as well. In Fig. 9.5 the 73.8 MHz phosphorus spectrum is obtained on a rat[44] using a surface coil placed on the live animal. The ATP resonances are broadened but readily detectable. One may observe in addition to inorganic phosphate the ^{31}P resonance of another important metabolite, phosphocreatine:

9.2 NMR IMAGING (L. W. JELINSKI)

9.2.1 Introduction

NMR imaging, also called MRI or *magnetic resonance imaging*, has become a valuable medical diagnostic tool. Medical applications of imaging evolved rapidly from Lauterbur's demonstration in 1973[45] of a two-dimensional NMR image from two water-containing 1-mm tubes whose centers were separated by 3.2 mm. Lauterbur proposed the term *zeugmatography* to describe this technique. From the Greek word *zeugma* meaning *that which is used for joining*, the term refers to bringing together the radio frequency field necessary to produce the NMR signal and the magnetic field gradients that produce the spatial encoding of this NMR signal.

NMR imaging is a noninvasive technique that generates images of "slices" of the human body, such as the one in Fig. 9.6. Since the magnet must be large enough to accommodate even obese humans, NMR imaging spectrometers for medical applications are massive. Figure 9.7 is a photograph of one such system. This figure shows a patient positioned on a tray that can be slid into the bore of the horizontal magnet. NMR images get their contrast from the differences in water concentration in various parts of the sample and because different tissues and tumors have different relaxation times (T_1 and T_2). For example, the proton content increases in going from bone to blood to muscle to fat to cerebrospinal fluid.[46] Furthermore, the relaxation times in these materials are very different. In general, the amount of water and the relaxation times of tumors are different from the surrounding tissue, also affording contrast.[47]

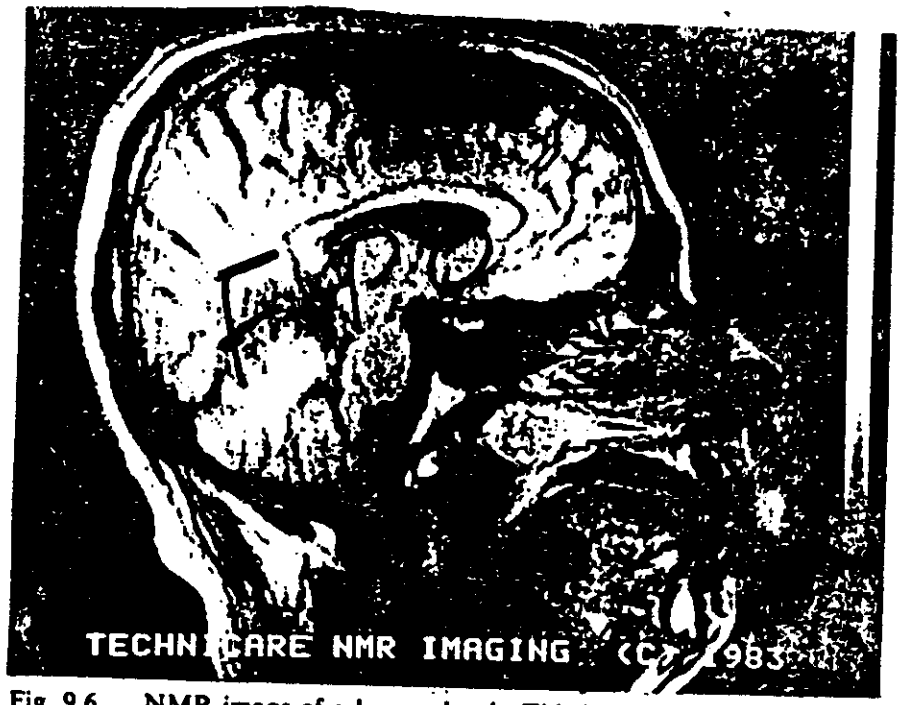

Fig. 9.6 NMR image of a human head. This is a *sagittal* image, or one that runs along a plane parallel to the plane through the nose and back of the head. *Coronal* images are parallel to the plane running from ear to ear. (Courtesy of Technicare.)

NMR imaging uses many of the concepts that we have already encountered, with one major difference. So far we have concentrated on homogeneity — homogeneous magnetic fields and homogeneous B_1 fields. These methods give average information about the composition of ostensibly homogeneous materials. For example, two capillaries of water placed side by side in a homogeneous magnetic field would produce a composite signal, a single line whose frequency, ω, is given by $\omega = \gamma B_o$ [see Fig. 9.8(a)].[46] (Controlled test samples such as these capillaries are often called *phantoms*.) However, if instead of a homogeneous magnetic field, the two capillaries were placed in a *magnetic field gradient* (produced by the coils shown in [Fig. 9.8(b)], the water in capillary A would resonate at a frequency different from that of capillary B. The frequency of peak A would be given by $\omega_A = \gamma B_A$, where B_A is the magnetic field at the position of capillary A. (A similar condition holds for capillary B.) Magnetic field gradients produce the spatial discrimination necessary for magnetic resonance imaging. The distance between two objects can be

Fig. 9.7 NMR imaging machine. (Courtesy of General Electric Company.)

determined if the field gradient is linear and if the rate at which it changes is known.

We can see that this simple analysis readily falls apart if we were to position the capillaries differently in the magnetic field [see for example, Fig. 9.8(c)]. In practice, one wants the x, y, and z coordinates of a particular volume element, and in order to avoid the confusion illustrated in Fig. 9.8c, various gradients along x, y, and z are used to produce images.

9.2.2 Imaging Methods

There are many techniques for obtaining an NMR image, and the interested reader is referred to Ref. 48 for a comprehensive review. Here we will present the rudiments of some of the more basic methods. These methods can be divided into four general classes according to the volume element that they sample.[49] This classification scheme is illustrated in Fig. 9.9. The methods range from building an image out of a number of single point measurements [Fig. 9.9(a)] to sequential measurement of a number of lines [Fig. 9.9(b)] to sequential build-up of a series of planar images [Fig. 9.9(c)] to obtaining the entire image at once [Fig. 9.9(d)] and then reconstructing the desired slice for visualization purposes.

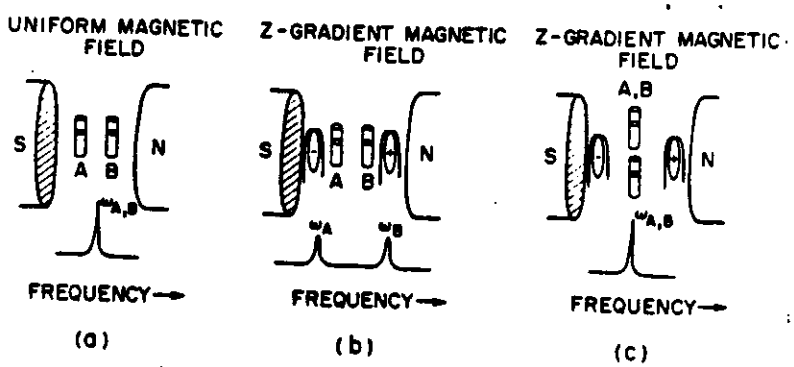

Fig. 9.8 (a) Two capillaries of water side-by-side in a homogeneous magnetic field produce a single line. In the presence of a field gradient these two capillaries produce separate lines (b) unless the capillaries experience the same gradient (c). [Adapted from J. D. Roberts, *Eng. & Sci.*, 10 (January 1986).]

9.2.2.1 Sequential Point Measurements

We have already seen that surface coils [Chapter 2, Fig. 2.13(c)] can provide information about the area immediately beneath them. The fall-off of the B_1 homogeneity of these coils determines the volume that they sample. Outside the region of B_1 homogeneity, the sample receives inadequate radio frequency excitation, and the signals from parts of the sample lying outside of this region are markedly diminished. In general the B_1 field inhomogeneity of these coils is such that they are selective for hemispheric regions of the sample that are within approximately the

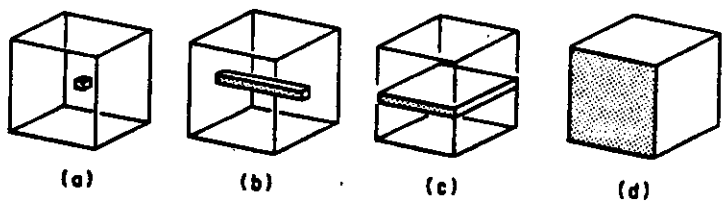

Fig. 9.9 Classification of NMR imaging methods according to the volume they sample: (a) sequential point measurement; (b) line measurement; (c) plane measurement; (d) volume measurement, or 3-D zeugmatography. [Adapted from *NMR: A Perspective on Imaging*, General Electric Corporation, Medical Systems Operations, Milwaukee, Wisconsin (1982).]

circumference of the coil and extending to a depth corresponding to one radius of the coil. Although various pulse sequences have been proposed to make these volumes more selective,[50] surface coils are generally best for observing chemical shift spectra (see Chapter 3) of localized regions of tissue. A two dimensional image plane could be built up by physically moving the surface coil over the surface of the sample.

A somewhat different technique involves creating high order magnetic field gradients so that the magnetic field is homogeneous over only a very small volume. In the rest of the region , the magnetic field homogeneity falls off very steeply, and thus signals from objects outside the sensitive region are extremely broad. It then becomes necessary to move the sample about in the magnetic field in order to build up the image scan.

Moving the coil around on the surface of the sample or moving the sample around within the magnetic field are tedious and inefficient ways to obtain an image. The *sensitive point* method[51] overcomes these drawbacks. This method relies on time-dependent magnetic field gradients along the x, y, and z directions. They produce a sensitive point that can be scanned along the sample by changing the magnetic field gradients. The way this works can be understood by looking first at the effect of one time-dependent magnetic field gradient, given by

$$(x - x_0)G_x \cos(\Omega_x t) \tag{9.2}$$

where x_0 describes the position, G_x the x-gradient amplitude, and Ω_x the frequency. This produces time dependence on the NMR signals from all regions of the sample except where $x = x_0$, the region where the time-dependent gradient vanishes. A special pulse sequence, to provide a steady state free precession signal, then excites the signal that arises from the sensitive plane, described by $x = x_0$. When gradients in the y and z directions are also added to this scheme, the time independent signal arises from the sensitive point given by (x_0, y_0, z_0). This sensitive point can then be moved about in the sample by changing the strengths of the magnetic field gradients.

Although not computationally demanding, the sequential point methods suffer from inefficiency and have been largely supplanted by planar and volume methods. The foregoing description is useful, however, for pedagogical purposes.

9.2.2.2 Line Methods

We have seen that one may build an NMR scan from an assembly of sensitive points. There are also a number of ways to obtain a scan by the sequential scanning of lines. We shall describe only one of them here, as

these, too, have been largely superseded by the more efficient planar and volume methods.

One of the sequential line methods involves an extension of the sensitive point technique.[52,53] The sensitive line is generated by creating two (instead of three, as in the sensitive point method) time dependent magnetic field gradients. Let us assume that they are along the x and y directions. As before, the NMR signal will be time-dependent from all regions except where $x = x_0$ and $y = y_0$. This provides a line that runs along z. In conjunction with the steady-state free precession pulse sequence, this produces a spectrum along the line defined by x_0, y_0. Discrimination of the signal along this line is accomplished by imposing a *static* magnetic field gradient along the z direction, thereby producing spatial encoding along this line. The scan is then built up by moving the position of this line across the sample.

9.2.2.3 Planar Methods

Lauterbur used the *projection reconstruction* method in his original report on capillaries of water.[45] This principle has been used extensively in other imaging methods, most notably in X-ray computed tomography (CT scans). A series of one-dimensional projections are obtained by incrementally rotating the magnetic field gradient through 180°.[54] The two-dimensional image is then reconstructed from these one-dimensional images using standard projection reconstruction algorithms borrowed from CT methodology. Figure 9.10 illustrates this process. In Fig. 9.10(a), the magnetic field B_0 is parallel to the magnetic field gradient G, which produces the one dimensional image shown at the bottom of the figure. The gradient G is then rotated to other positions and other one-dimensional images such as the ones in (b) and (c) are obtained. The spatial arrangement of the objects is then back-calculated to produce the image shown on the right-hand side of the figure.

Up until now we have ignored the problem of *slice selection*. Lauterbur's projection reconstruction image relied on the receiver coil geometry for crude control of the slab or slice thickness. Slice selection is now generally controlled by a tailored, frequency-selective radio frequency pulse that is applied in the presence of a field gradient perpendicular to the plane of the desired slice [see Fig. 9.11(a)]. Both the strength of the magnetic field gradient and the frequency bandwidth (see Chapter 1, Section 1.4, and Chapter 2, Section 2.4.3) of the selective 90° radio frequency pulse control the slice thickness. Figure 9.12 illustrates these effects.[55] In (a) the frequency bandwidth, $\Delta\omega_0$, is kept constant and the gradient strength is varied from a steep gradient (illustrated by the line

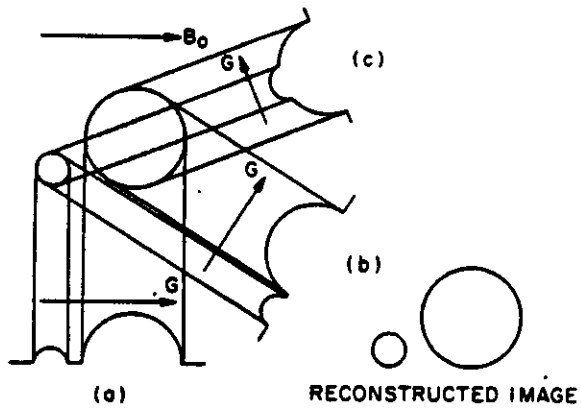

Fig. 9.10 Method of obtaining one dimensional images for the projection-reconstruction technique. The magnetic field gradient, G, is rotated about the sample. When G is parallel to the magnetic field, B_0, the image in (a) is produced. Other one dimensional images are shown in (b) and (c). The reconstructed image is shown.

A), which gives a slab of thickness Δz_A, to a lower gradient (the line B), which produces a thicker slice. If the gradient is kept constant [Fig. 9.12(b)], a more selective radio frequency pulse ($\Delta\omega_A$) produces a thinner slice (Δz_A).

Having described methods for slice selection, we address another class of planar methods of imaging. These include two dimensional NMR Fourier zeugmatography,[56,57] rotating frame zeugmatography,[58] the echo planar method,[59] and spin warp imaging.[60] All of these methods bear a formal similarity to the two dimensional NMR methods that we have already seen (Chapter 6) in that they involve preparation, evolution, and acquisition time periods. It is beyond the scope of this book to describe all of these methods, so we shall concentrate on one of them, the spin warp technique. A description of this method illustrates the principles of phase encoding, which are common to many two- and three-dimensional techniques.

A simplified version of the spin warp technique is shown in Fig. 9.11. The preparation period consists of selective excitation of the desired plane using a tailored 90° radio frequency pulse [Fig. 9.11(a)]. Phase encoding is produced by applying a gradient in the y direction. This gradient causes

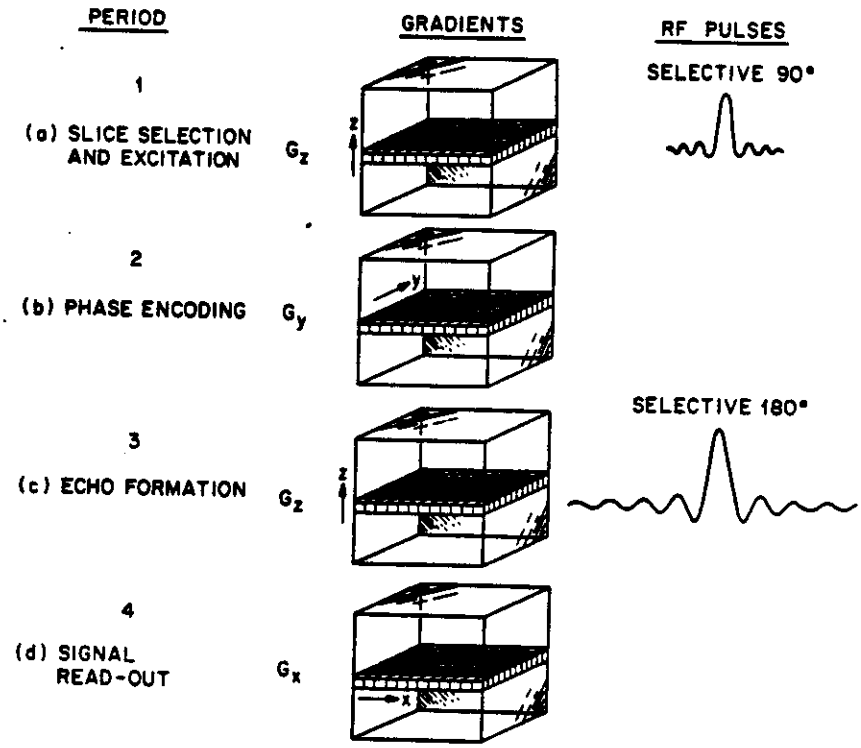

Fig. 9.11 Basic time periods in measuring an NMR image. (Adapted from F. W. Wehrli, J. R. MacFall, and T. H. Newton in *Advanced Imaging Techniques*, T. H. Newton and D. G. Potts, Eds., Clavadel Press, San Anselmo, California, 1983, pp. 81–117.)

the nuclei across the sample to precess at frequencies that are characteristic of their location with respect to the G_y gradient. (For now we shall assume that there is only one chemical species, i.e., water, contributing to the image.) At the end of this period, each of the volume elements has accumulated a phase angle that is directly related to its position in the gradient. Figure 9.13 illustrates the principle of phase encoding for three volume elements *A*, *B*, and *C* in a G_y gradient. At time $t = 0$, the nuclei in these volume elements have been polarized by the selective excitation pulse and lie in the *x y* plane. Since the nuclei in these volumes experience different magnetic fields due to the G_y field gradient, they precess at different frequencies. At the end of the G_y gradient at $t = \Delta t_y$, the magnetic moments from each of the volume elements have precessed through an angle related to their position in the G_y gradient.

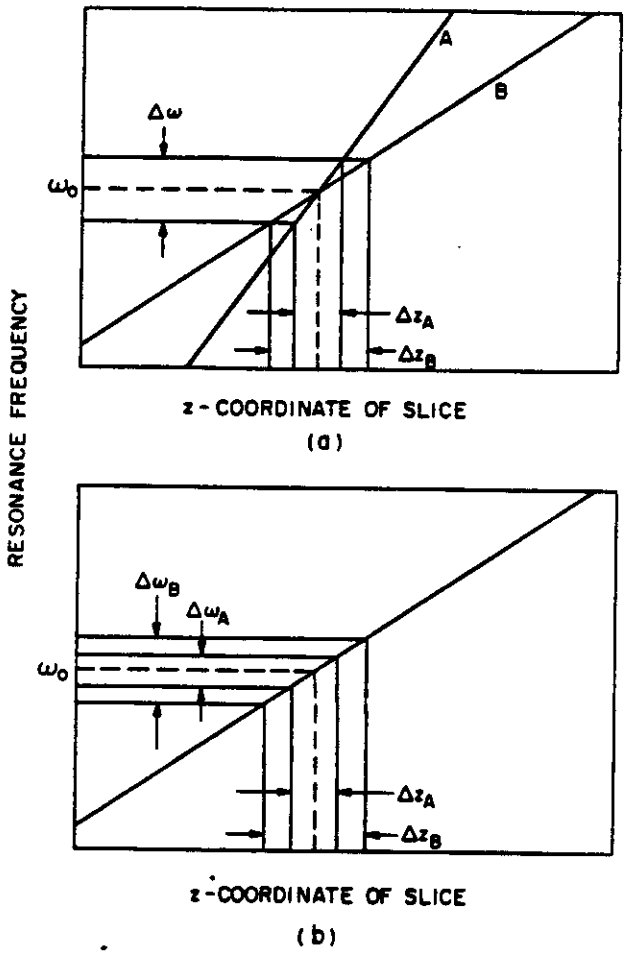

Fig. 9.12 Illustration of the effect on the slice thickness of variations in the strength of the magnetic field gradient (a) and the bandwidth of the selective radio frequency pulse (b).[55] In (a), the steeper field gradient A produces the narrower slab, Δz_A. In (b), the narrower bandwidth pulse $\Delta\omega_A$ produces the thinner slice.

The third period shown in Fig. 9.11(c) is composed of a selective 180° pulse (again, with the G_z gradient on), which accomplishes the second part of the T_2 ($90° - \tau - 180°$) spin echo pulse sequence (see Section 5.3). Because of this 180° pulse, an image obtained with this pulse sequence would be called a *T_2 image*. A *T_1 image* could be obtained instead by

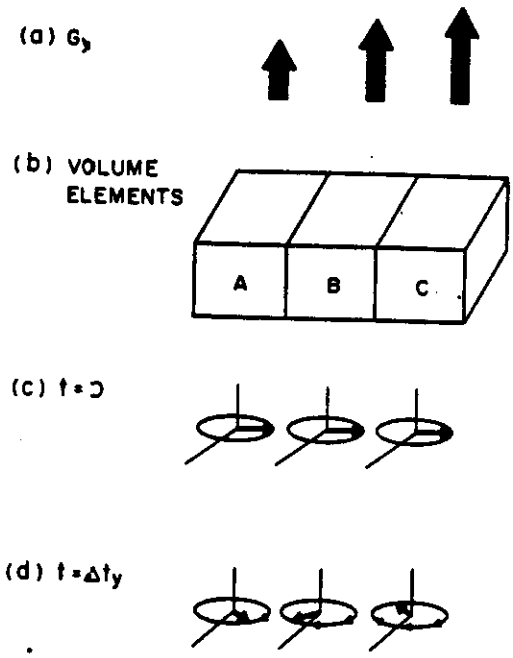

Fig. 9.13 In the presence of field gradients, G_y, the volume elements A, B, and C will initially have identical phases (c), but at the end of the gradient period, the spins in these elements will have accumulated different phases (d). (Adapted from F. W. Wehrli, J. R. MacFall, and T. H. Newton in *Advanced Imaging Techniques*, T. H. Newton and D. G. Potts, Eds., Clavadel Press, San Anselmo, California, 1983, pp. 81–117.)

performing a nonselective 180° pulse prior to the slice selection part of this sequence. The last part of the image acquisition process [Fig. 9.11(d)] involves signal readout, this time in the presence of the third gradient.

In order to obtain an image of, for example, 128 × 128 picture elements, or *pixels*, it is necessary to obtain 128 different free induction decay signals, each one differing from the others by an incremental value of the phase encoding gradient, G_y. These FIDs are then transformed with respect to the read-out coordinate, x, then transposed and Fourier transformed with respect to the phase encoding gradient in a fashion analogous to the two-dimensional Fourier transform techniques described in Chapter 6 (see Fig. 6.1).

The description of the spin warp technique given in Fig. 9.11 shows only the main features of the select – encode – read sequence. A more complete description is shown in Fig. 9.14. The tailored 90° excitation

The description of the spin warp technique given in Fig. 9.11 shows only the main features of the select – encode – read sequence. A more complete description is shown in Fig. 9.14. The tailored 90° excitation pulse for slice selection can be of a $(\sin x)/x$ form convoluted with a gaussian. The G_z gradient is on during this time. Immediately following the slice selection, the G_z gradient is inverted, producing time reversal, which rephases the spins. An inverted x gradient is also applied and acts to advance the position of the echo along the time axis and away from the time of the pulses. Simultaneously, the G_y phase encoding gradient is applied. (The amplitude of this gradient is incremented for each successive scan.) A 180° selective radio frequency pulse is then applied to the G_z-selected slice. The purpose of this pulse is to provide the Hahn echo (see Chapter 5, Section 5.3) that will provide the T_2 contrast necessary for the image. The G_x gradient is then turned on during the time that the spin echo is being detected.

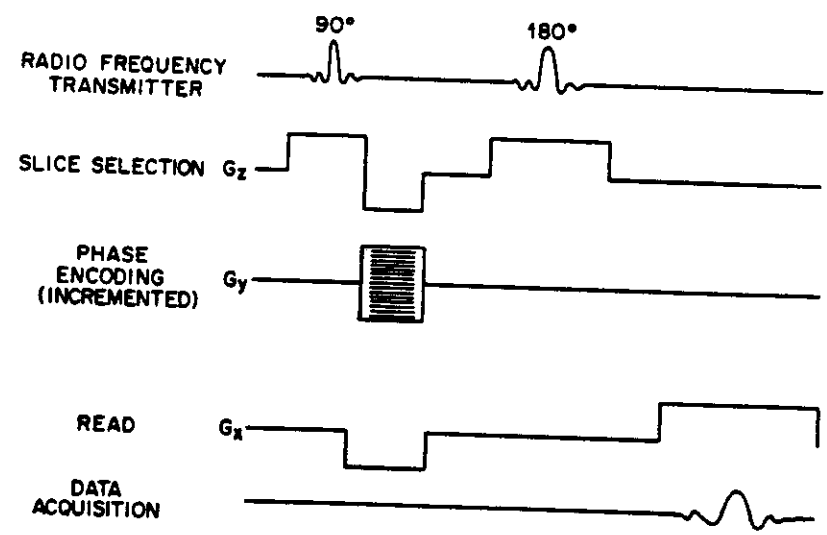

Fig. 9.14 Pulse sequence for a T_2 image acquired with the spin warp technique.

The relatively long T_1 of water in biological tissues (hundreds of milliseconds) usually governs the repetition rate of the data acquisition, and therefore the rate at which the G_y gradient is incremented. *Multislice imaging* is a way around this. This method involves cycling through scans of different slices at the same value of G_y while waiting for the protons in the first slice to relax. This method affords an enormous time savings and makes the difference between clinically reasonable and clinically infeasible NMR images.

9.2.2.4 Three-Dimensional Techniques

Data can be collected simultaneously from the entire imaging volume using three-dimensional techniques.[57] The methods for performing this are based on an extension of two dimensional imaging. Instead of selecting a slice with a slice-selective pulse, the entire volume is excited. A variable phase encoding gradient, G_z, is applied to separate the protons along the z axis, and a G_y gradient is simultaneously applied to differentiate the protons along the y direction. At the end of this phase-encoding period, the signal from each *voxel* (the three-dimensional equivalent of a pixel) element has a phase that is related to its position with respect to the y and z axes. The signal is then read out with a G_x static gradient. Fourier transformation is then performed with respect to G_x and then with respect to the two phase encoding gradients, G_y and G_z. Although computationally intensive, this method produces data that can be reconfigured to trace out the shape and size of tumors or other objects in three dimensions.

9.2.3 Relaxation and Contrast Enhancement in Imaging

9.2.3.1 Water Content and Relaxation

The protons in biological tissue exist in widely diverse environments. For example, there are protons in water, bone, fibrous proteins that make up the skin, lipids, blood, and DNA. Of these components, the protons in water and lipids are the primary contributors to the NMR image. The protons in bone and large proteins, because they have long correlation times, generally produce signals that are so broad that they are not observed in the NMR image. Although there are differences in the proton content in various parts of the body, the density of protons is not the major factor controlling the relative contrast observed in an image. Instead, most of the contrast in an NMR image depends on differences in the T_1 and T_2 of various tissues.

We have already examined the fundamental processes leading to nuclear relaxation (see Chapter 1, Section 1.7, and Chapter 5, Section 5.3). These fundamental principles apply to relaxation in NMR imaging.

For example, of the two major contributors to the NMR image signal, we would expect that water would have a longer T_1 than the lipids, since the water is a smaller molecule and will have a shorter correlation time. (Recall that relaxation is most efficient when $\omega\tau_c = 1$; see Fig. 1.8.) However, the water molecules in biological tissue have relaxation times that are far shorter (i.e., relaxation is more efficient) than is observed for bulk or free water. This shortening of the relaxation time arises because part of the water exists in a "bound" state, where it is associated with protein or DNA macromolecules. This temporarily immobilized water exchanges with the bulk water, in effect producing an averaged relaxation time for the water in a particular tissue or tumor. Therefore, the T_1 of water in biological tissues is of the order of hundreds of milliseconds, rather than the order of seconds, as it is in bulk or free water. It is thought that the exchange between free and bound water is affected in certain pathological conditions, perhaps because proteins are present in differing amounts, or because different proteins are produced.[61] Differences in water exchange lead to differences in T_1, which lead to differences in the contrast of an image.

Recall also that T_2 processes involve the loss of transverse magnetization (M_x and M_y), and that this decay in magnetization happens because the nuclear magnetic moments get out of phase with each other. We have already seen that many processes contribute to this dephasing, most notably magnetic field inhomogeneities. These magnetic field inhomogeneities can arise from the static magnetic field or from field inhomogeneities generated by the tissues themselves. We have already seen (Chapter 5, Section 5.3) that T_2 relaxation is most efficient for large molecules with long correlation times. As is the case with T_1 relaxation, the T_2 for bound water is much shorter than for free water, thereby affording image contrast.

The standard pulse sequences we have already seen [T_1 by inversion-recovery (Chapter 5, Fig. 5.5), partial saturation, and T_2 by spin echo (Chapter 5, Section 5.4.7.)] can be used with slice-selection pulses and gradients to produce what are known as "T_1" and "T_2" images. The pulse sequence diagram in Fig. 9.14 illustrates how a T_2 image would be obtained.

Much research has been performed to determine the conditions for obtaining optimum contrast in medical images. The interested reader is referred to Ref. 55 for an excellent overview of the subject.

9.2.3.2 Contrast Enhancement Agents

We have already seen that relaxation reagents, usually paramagnetic materials, are added to samples for high resolution NMR to enhance T_2

relaxation (see Chapter 2, Section 2.7.1). Relaxation reagents, generally known in medical imaging as *contrast agents*, can be employed to enhance the appearance of images and to facilitate diagnoses.[62] Most of these reagents are based on paramagnetic ions such as manganese or gadolinium, or on stable nitroxide free radicals. The ideal reagent is tissue specific, nontoxic, and rapidly excreted from the body without undergoing metabolism to other materials. Such reagents have been used, for example, to determine whether or not the blood–brain barrier is intact. Nitroxides have been shown to accumulate where there is damage to the blood–brain barrier and they produce enhanced relaxation in these regions.[62]

Monoclonal antibodies with covalent or chelated paramagnetic ions have been employed as tissue-seeking contrast enhancement reagents.[62]

9.2.4 Imaging of Flow

It has long been recognized that NMR spectroscopy can be used to measure flow, and these principles have now been extended to NMR imaging. The basic idea is that the slice-selection pulse excites only those spins in the slice, as before. However, some fraction of these saturated spins flow out of the excitation slice by the time the signal is detected. In their place in the slice are "fresh" spins – spins that have not been saturated by the initial radio frequency pulse (see Fig. 9.15). The contrast

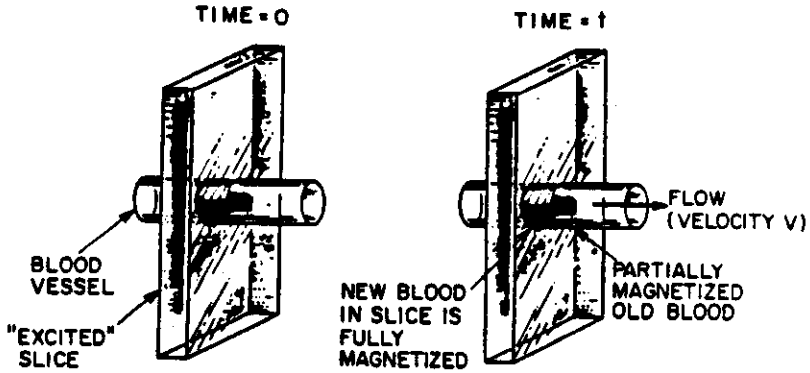

Fig. 9.15 (a) At time = 0, the slice selection pulse "tags" the nuclei in the slice. (b) When the signal is detected at a later time t both the fresh and "tagged" blood in the imaging slice will be detected. (Adapted from F. W. Wehrli, J. R. MacFall, and T. H. Newton in *Advanced Imaging Techniques*, T. H. Newton and D. G. Potts, Eds., Clavadel Press, San Anselmo, California, 1983, pp. 81–117.)

Fig. 9.16 Flow image of the thighs of a normal subject: sfa, superficial femoral artery; dfa, deep femoral artery. [Adapted from V. J. Wedeen, R. A. Meuli, R. R. Edelman, S. C. Geller, L. R. Frank, T. J. Brady, and B. R. Rosen, *Science* **230**, 946 (1985).]

depends on the blood flow rate and upon the time between the slice selection pulse and the "read" pulse. If new blood is flowing into the slice, it will have a greater signal strength than the blood that was originally there, as the new blood is fully magnetized, whereas the old blood, depending on the time between pulses, is still partially saturated.

The foregoing is a very simplified description of the use of NMR to measure flow. Actual experiments are generally more complicated and use electrocardiographic gating of signal acquisition and signal subtraction techniques together with velocity dependent phase shifts.[63] These velocity dependent phase shifts are caused by the x gradient pulses, which simultaneously perform the spatial encoding in x. Using these methods, vessels as small as 1 —.2 mm in diameter can be detected in a 50-cm field of view in less than 15 min. Figure 9.16 shows a flow image of the thighs of a human, where the superficial femoral artery (sfa) and the deep femoral artery (dfa) are clearly seen. These NMR measurements of flow are completely noninvasive and do not require arterial catheterization as does Roengten angiography. Furthermore, they can be used in cranial regions, where other techniques, such as ultrasonography, provide insufficient resolution.[63]

9.2.5 Chemical Shift Imaging

So far in our discussion of NMR imaging we have assumed that we are observing one chemical shift, i.e., that of water. In reality, the major contributors to the NMR image, water and lipids, have chemical shifts that differ by several parts per million. These differences in chemical shifts will manifest themselves as differences in spatial position in an NMR image. At low magnetic field strengths (less than about 1 tesla) these so-called *chemical shift artifacts* are not a problem, since the lipid and water components produce a composite signal. However, at higher magnetic field strengths, the signals from water and from lipid will produce "ghosts." A number of techniques have been proposed to avoid the problems of chemical shift artifacts.

It is also possible to exploit these chemical shift differences in a method known as *chemical shift imaging*. This is, in essence, a form of four-dimensional imaging, with three of the dimensions being spatial and the fourth being the chemical shift.

There are several techniques that will produce a chemical shift image. For example, the projection reconstruction method can be used to obtain a chemical shift spectrum for each point in the projection.[48] Each point is obtained with a selective excitation pulse, applied in the presence of an appropriate field gradient. The signal is then detected in the absence of a field gradient. In another more complicated method, a slice is selected with an appropriately shaped radio frequency pulse, a nonselective 90° pulse is applied, and the G_x, G_y, and G_z gradients are used to spatially encode the signal. The free induction decay signal is then recorded in the absence of a field gradient. The free induction decay is then transformed with respect to the gradients to give the three-dimensional spatial information and with respect to the acquisition time to give the fourth dimension of frequency (i.e., chemical shift).

A more detailed description of chemical shift imaging is beyond the scope of this section, and the interested reader is directed to Ref. 64 for more details about this and other imaging methods. However, it is important to note that techniques such as chemical shift imaging may become potentially useful techniques in the diagnosis of certain disease states.[65]

9.2.6 Imaging of Solids and Materials

Up until now our description of NMR imaging has centered about imaging of protons, and in particular, the protons from water and from lipids. Protons from these substances generally have narrow linewidths, owing to their nearly isotropic motion. The lines are narrow because this

rapid motion averages out the local dipolar fields. As we have already seen (Chapter 8, Section 8.2), these fields are very large in solids, but can be removed by applying a field that is large compared to the interaction strength (i.e., dipolar decoupling). Because these fields can be as large as 5 G, a gradient greater than 50 G/cm would be needed to achieve a resolution of 1 mm.[66] One way to circumvent this problem in NMR imaging is to use multiple-pulse line narrowing (Chapter 8, Section 8.7), or to use it in combination with multiple quantum NMR.[66] An alternate method involves eliminating the line broadening effects by observing the free induction decay signal at a fixed time while the experiment is repeated, each time with incremented field gradient steps.[67] This latter method has been applied to solid adamantane.

There are certain problems in materials science that can be solved without going to these line-narrowing techniques. For example, NMR imaging can be used to determine the uptake patterns of water in epoxy resins, follow the time dependence of polymer curing (going from a liquid or mobile material to a solid), or monitor the distribution of oil in a solid sample.

9.3 SOLVENT SUPPRESSION (P. A. MIRAU AND F. A. BOVEY)

9.3.1 Introduction

It may happen in solution NMR that the resonance of the solvent itself, which is usually present in great molar excess over the solute, is inconveniently large, and may mask solute resonances of interest or cause dynamic range problems (see Chapter 2, Section 2.5.2). In carbon−13 spectroscopy this is seldom a difficulty because of the large range of chemical shifts; if a particular solvent has interfering resonances one chooses another. The most serious problems arise in the study of biomolecules, where H_2O and D_2O are often necessarily the solvent of choice. Since H_2O is *ca.* 55 molar, its proton resonance, appearing near 5 ppm, overwhelms all others. Even when employing D_2O, the residual HDO peak is likely to be inconveniently large and in addition one loses the rapidly exchangeable solute proton resonances. It is therefore often desirable to either (a) saturate the solvent resonance or (b) selectively excite the solute resonances. There have been many proposals for accomplishing solvent resonance suppression by one or the other of these approaches, and we shall discuss some of the more effective procedures.

9.3.2 Solvent Saturation

The simplest scheme is to apply a proton field using the proton decoupler for a sufficient time and at an appropriate power level [see

Chapter 1, Eq. (1.50)] to saturate the solvent resonance. The decoupler is then shut off, a 90° pulse applied, and the solute spectrum acquired. This will not work if solute resonances of interest are under or very close to the solvent peak, or if such resonances represent protons that are in exchange with the solvent. In the latter case, the solvent saturation will be transferred to the solute in the manner we have already described (Chapter 5, Section 5.4.7.1.) It is in general best to use minimum field strength for the shortest time that gives adequate suppression.

9.3.3 Solvent Nulling and Selective Excitation

9.3.3.1 WEFT

The acronym stands for *W*ater *E*liminated *F*ourier *T*ransform NMR spectroscopy.[68] This method is based on the inversion-recovery technique for the measurement of the spin lattice relaxation time, T_1. We have seen (Chapter 5, Section 5.2.7.2) that this involves the inversion of the magnetization — in this case both the solvent and solute resonances — by a 180° pulse followed after an interval τ by a 90° sampling pulse to measure the regrowth of the magnetization toward equilibrium. We have further seen (Eq. 5.36) that when $\tau = \ln 2 T_1$ (solvent), or 0.693 T_1 (solvent) the recovering solvent magnetization passes through zero. If the solute T_1 is substantially shorter than that of the solvent, a 90° pulse at this time, followed by acquisition of the signal, will provide a spectrum of the solute without that of the solvent. After an interval of *ca.* $5T_1$ (solvent), the pulse sequence may be repeated.

Actually, it has been found that for HDO, it is not necessary in practice that T_1 (solvent) be greatly in excess of T_1 (solute); the condition T_1 (solvent) $\geq$ 1.4 T_1 (solute) has been found sufficient.[69]

In Fig. 9.17 is shown the 100 MHz proton spectra of threonine, $CH_3CHOHCH(NH_3^+)CO_2^-$, in D_2O[68] (details in the figure caption). Spectrum (a) is the normal spectrum with the strongly dominant HDO resonance at *ca.* 5.2 ppm; in (b) is the WEFT spectrum, exhibiting an at least 1000-fold suppression of the solvent resonance.

9.3.3.2 The Redfield "2-1-4" Pulse

A frequently employed method for the selective excitation of solute resonances without exciting the solvent is the Redfield "2-1-4" pulse.[70,71] This is an example of a *composite* pulse, i.e., one in which the phase of B_1 is shifted during the pulse without the insertion of intervals. In order to understand the operation of this pulse one must realize that even in the absence of a resonating nucleus the rf pulse itself has a Fourier transform. For a square-wave pulse this is of the form sinc x, i.e., $(\sin x)/x$, a function having a central maximum with an infinite train of diminishing wiggles on each side:

Laboratory, 7, 34-41 (1989)

NMR Imaging: From whole bodies to single cells

BY L.W. JELINSKI, R.W. BEHLING, H.K. TUBBS, AND M.D. COCKMAN

THE OBJECT in *Figure 1* can easily be identified as a slice of orange. This photograph is exciting because it is not a physical slice of the orange, but rather is an NMR image of a whole orange that had a notch cut in its side. The slice was obtained without physical damage to the orange. The ability to obtain noninvasive slices of objects has created great interest in the medical field, and this interest has fueled rapid development of many medical and nonmedical applications. Through NMR imaging, major advances are being experienced in the ability to diagnose pathological conditions and in the ability to obtain new chemical information about living systems.

The first NMR image was reported only slightly more than a decade ago.[1] Although there is still some contention about who first invented NMR imaging,[2] there is no question about the value of this technique. There is also some disagreement about what to call it. Lauterbur originally proposed zeugmatography, from the Greek meaning that which is used for joining, referring to the bringing together of the radio frequency signal that is needed to obtain the NMR information and the magnetic field gradients needed to produce the spatial information. The suggested nomenclature did not catch on, and those trained in nuclear magnetic resonance called it NMR imaging in its early days, whereas those in the medical profession correctly recognized that the word "nuclear" might make the public uneasy. The medical community generally uses MRI for magnetic resonance imaging. The technique, however, has nothing to do with radioactivity, and the word nuclear refers to the nucleus of the atom, in most cases the nucleus of the hydrogen atom in water. (The terms MRI and NMR imaging will be used interchangeably in this article.)

The Food and Drug Administration first licensed MRI for human patients in 1983, although it was used several years before that on an experimental basis. It was only in 1985 that hospitals were generally reimbursed for MRI services.[3] Currently, nearly every major medical center performs MRI, and MRI clinics exist in suburban areas throughout the country. In 1987 approximately two dozen companies worldwide sold over 500

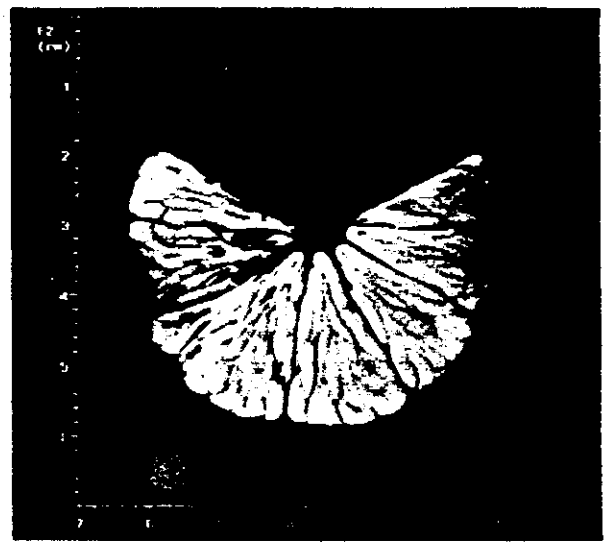

Figure 1 *Proton NMR image (7.0 Tesla, 300 MHz) of a 2-mm slice of a navel orange that had a notch cut in it. Notice that the seeds, membrane structures, and features of the peel are visible in this presentation.*

MRI systems to hospitals and clinics.[3] At an average of $1.5 million each, industry sales are estimated at $750 million. Furthermore, there were 3000 attendees at the 1988 meeting of the Society of Magnetic Resonance in Medicine, a Society that has been in existence only since 1981.

Why have we seen such rapid growth in the acceptance of this technique? There are clearly many factors, but the main one is because MRI images provide noninvasive, nondestructive information that is difficult to acquire or is otherwise unobtainable. Furthermore, the medical information is often complementary to that from CT (computerized tomography) scans. Magnetic resonance imaging uses no ionizing radiation and is best for soft tissues and tumors, whereas CT scans highlight the bone and mineralized structures. Because it senses water, MRI is particularly good for discovering growths that are hidden by bone.

Scope

This article provides an overview of the field of NMR imaging for the nonspecialist. The paper begins with a brief description of how NMR and NMR imaging work, in which a general conceptual and physical understanding of the technique will be conveyed. Several examples from the authors' own work and from the recent

Dr. Jelinski is Head of the Molecular Biophysics Research Dept., Dr. Tubbs is Technical Staff Member and medical resident, and Dr. Cockman is Postdoctoral Technical Staff Member, AT&T Bell Laboratories, Murray Hill, New Jersey. Dr. Behling is a research scientist, Squibb Institute for Medical Research, Princeton, New Jersey. *The authors are grateful to Rick Wright of AT&T Bell Laboratories and to Lynette Corning of the Society of Magnetic Resonance in Medicine for providing us with business-related information, and to our unnamed colleague for kindly letting us use the MRI images of his brain.*

The NMR phenomenon springs from energy transitions in a magnetic field[a]

A nucleus with spin ½ (for example ^1H, ^{13}C, or ^{19}F) has two spin energy levels that are degenerate in the absence of a magnetic field. When this degeneracy is lifted by applying a magnetic field B_0, the energy difference between the levels, ΔE, is related to the magnetic field strength and the magnetogyric ratio, γ. The population of the energy levels is dictated by the Boltzmann distribution.

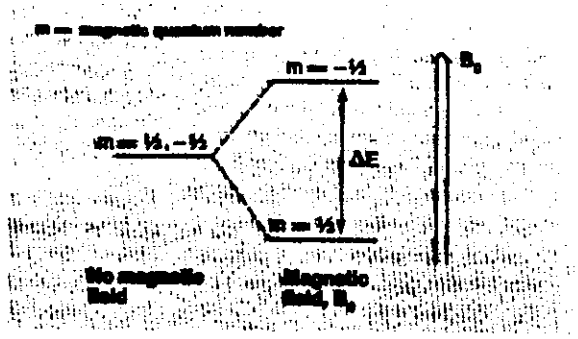

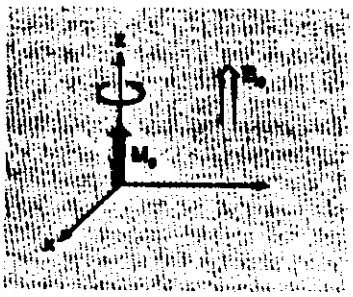

Viewed in a frame of reference rotating at the Larmor frequency, there is an excess net magnetization (M_0) along the field direction.

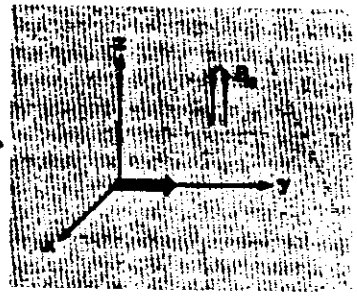

The NMR experiment consists of disturbing this equilibrium, generally with a burst of radio frequency energy called a 90° pulse.

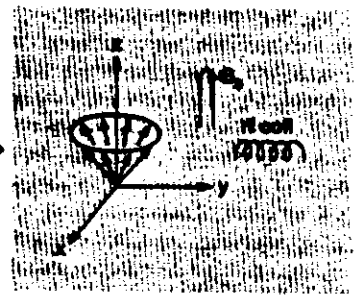

The spins dephase according to their chemical shifts. The spin system strives to re-establish its equilibrium via spin-spin (in the x-y plane) and spin-lattice (along z) processes.

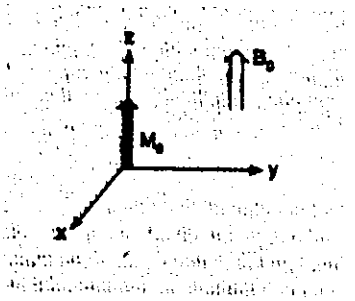

Equilibrium magnetization is eventually re-established and cycle can be repeated.

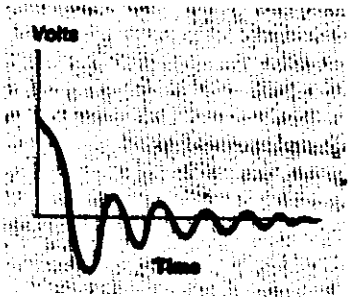

Meanwhile, the induced voltage is monitored in the x-y plane by a resonant radio frequency coil. This signal is the free induction decay (FID).

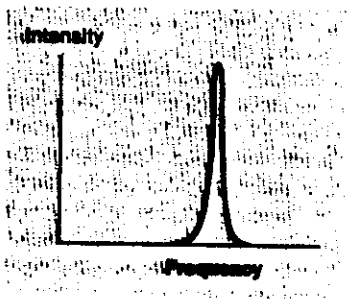

The FID is Fourier transformed to give the desired frequency-domain spectrum.

[a]*Reprinted from reference 4 with permission of the American Chemical Society.*

literature will be provided. Although by no means inclusive, these examples illustrate the rich diversity of systems that have been studied by NMR imaging. These applications range from the observation of a single cell, albeit a large one, to imaging slices of a human brain. Finally, the article concludes with a summary of the authors' thoughts on the future prospects for MRI.

Principles

The basic principles of NMR spectroscopy have been reviewed in many articles.[4-7] An inset outlines the main concepts behind NMR spectroscopy.[4]

Three main requirements exist for obtaining an NMR spectrum, as the name nuclear magnetic resonance implies. The *nuclear* part refers to the nuclear spin of the nucleus, such as ^1H, ^{31}P, ^{19}F, etc., which provides the signal. Although many nuclei can be imaged, this article discusses primarily NMR images of protons in water. As the term *magnetic* implies, a strong magnetic field is also required. The magnetic field strength of many medical imagers is between 1.4 and 2.0 Tesla, whereas research imagers are now made that exceed 8.4 Tesla. (For reference, Earth's magnetic field is 5×10^{-5} Tesla.) Many of the magnets used for NMR imaging employ superconducting magnet technology. As shown in the inset, the magnetic field lifts the degeneracy of the nuclear spin energy levels, and the spins precess about the magnetic field at the Larmor frequency, ω, given by:

$$\omega = \gamma B_0$$

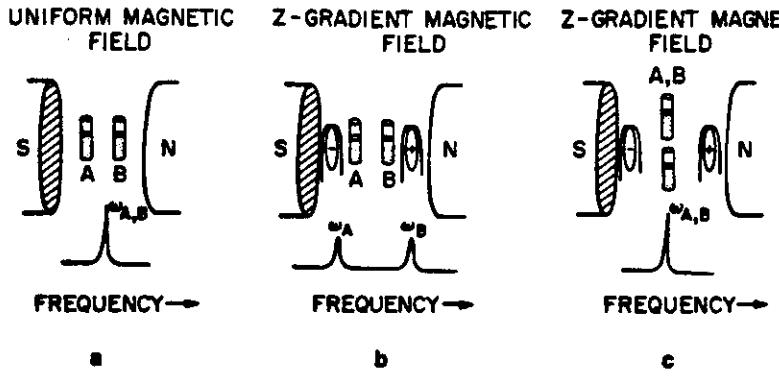

Figure 2 *a) Two capillaries of water, side-by-side in a homogeneous magnetic field produce a single NMR line. In the presence of a magnetic field gradient b), these two capillaries produce separate lines unless (c) the capillaries experience the same gradient. [Adapted from J.D. Roberts, Eng. & Sci., 10 (January 1986).]*

where γ is the magnetogyric ratio and B_0 is the magnetic field strength. *Resonance* occurs when an auxiliary electromagnetic field, B_1, is applied, the frequency of which exactly matches the frequency given by the energy difference between the nuclear spin energy levels (see inset). This auxiliary field is in the FM radio frequency range. (For example, 300 MHz was used to excite the proton nuclei for the image of the orange.)

The inset shows how an NMR spectrum can be obtained which consists of a plot of intensity versus frequency. These ideas can be extended to obtain a two-dimensional (2-D) plot of signal intensity versus spatial location. (The basics of NMR imaging have also been the subject of numerous review articles,[8-14] and this article provides only the main concepts.) Using the Larmor equation ($\omega = \gamma B_0$), spatial information can be obtained by imposing a known magnetic field gradient on the sample so that different regions in space experience slightly different magnetic fields. This causes them to resonate at different frequencies (see *Figures 2a* and *b*). However, problems arise if two regions of the sample experience the same magnetic field gradient (Figure 2*c*), or if a slice of the sample is selected.

In most implementations, NMR imaging requires magnetic field gradients in the *x*, *y*, and *z* directions. To obtain an image, the slice must first be selected. Suppose a coronal image of a slice of a patient's head that runs through the eyes is required. If a linear, known magnetic field gradient, G_z is applied, as shown in *Figure 3*, it will cause different coronal slices of the patient's head to resonate at different Larmor frequencies, ω_1, ω_2, and so on. To obtain information about the desired slice (ω_3, in this case), a highly selective, tailored[15] 90° radio frequency pulse that is of frequency ω_3, is applied. This excites only the spins in the slice shown in Figure 3. The thickness of the slice depends upon the strength (steepness) of the magnetic field gradient in the *z* direction and the bandwidth of the radio frequency pulse. The spatial information in the *xy* plane must then be obtained. This is done using a technique called *phase encoding*, and involves collecting a series of spectra (usually 128 or 256) that differ from one another by the size of the phase encoding gradient, G_y. The data are obtained by an echo method, usually either a spin echo or a gradient echo. *Figure 4* shows a spin echo pulse sequence, in which a 180° radio frequency pulse (also selective only for the desired slice) is used to refocus the magnetization. The echo is collected in the presence of the third gradient, G_x.

The contrast (shading) in NMR images arises from

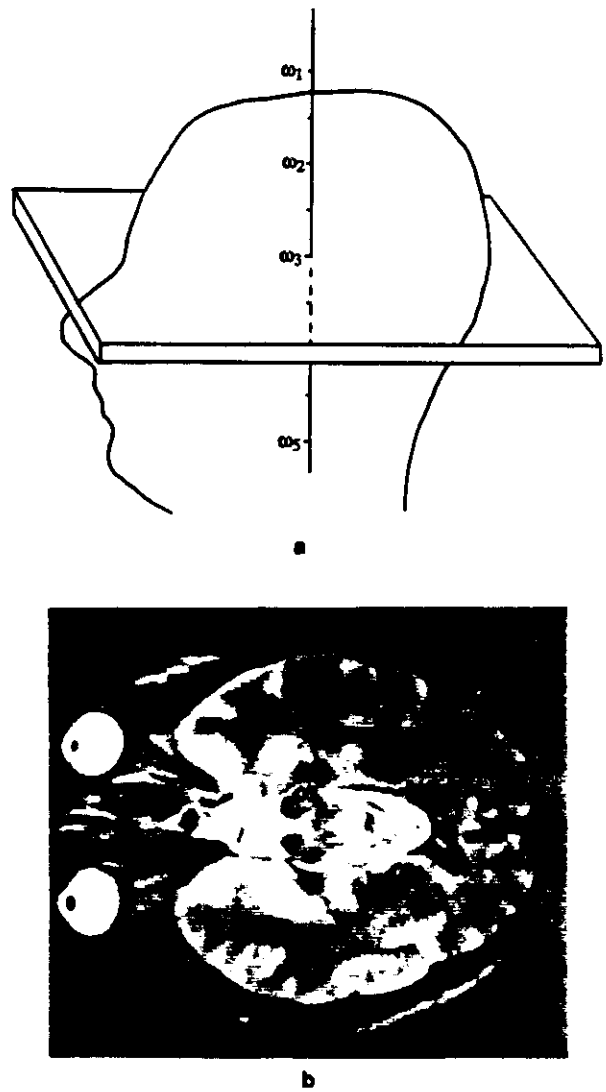

Figure 3 *a) The principle of slice selection. A linear magnetic field gradient G_z, causes different coronal planes to resonate at different frequencies (ω_1, ω_2 etc.). The slice defined by ω_3 can be chosen by using a selective radio frequency pulse to excite only the nuclei in that slice. The NMR image corresponding to this slice is shown in b).*

two main sources. One is simply the amount of water present in a particular tissue. The other source of contrast is related to the relaxation times, T_1 and T_2 (see inset) of the water nuclei, and can be used to great advantage to enhance one or another part of the image.[16] In general, the signal intensity, *S*, at any point in an

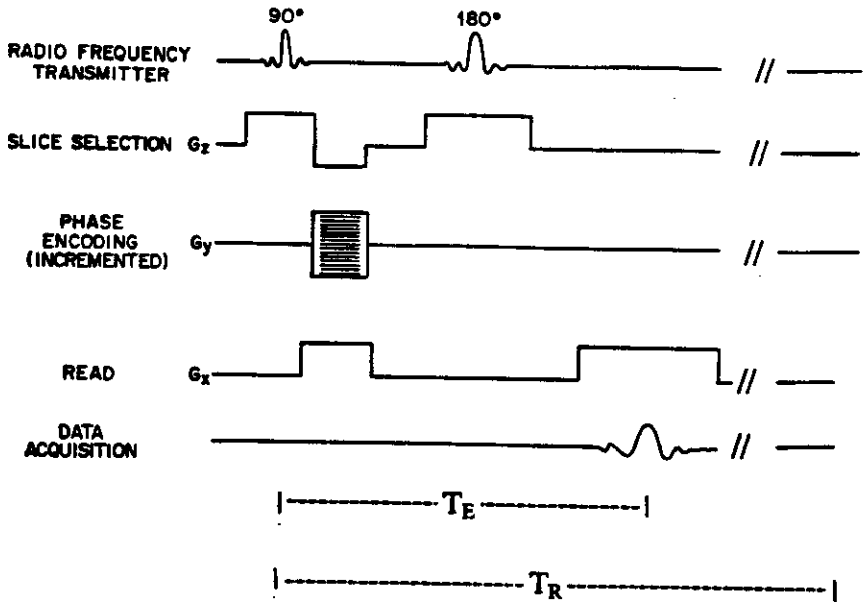

Figure 4 *The spin echo pulse sequence used for NMR imaging, showing the spin manipulations as a function of time. The top row shows the radio frequency pulses. These tailored pulses, in the presence of the slice selection gradient (second row), choose the plane of interest. The spatial information in the x-direction is obtained by acquiring the echo in the presence of the read gradient, G_x (fourth row). One echo is acquired for each value of the phase encode gradient, G_y. The y-gradient produces the spatial information in the y-direction of this plane. The negative-going slice-select gradient compensates for imperfections in the slice selection. The read gradient is turned on during phase encoding so that information is properly refocussed during echo acquisition. Typical times for the 90° pulse are 2 msec, for T_E are 20-90 msec, and for T_R are 1-5 sec.*

Figure 5 *Images of a coronal slice of a brain showing the effects of relaxation weighting. The image in a) is "T_2 weighted." It was acquired with a long T_E (90 msec) to highlight those structures that have long spin-spin relaxation times. The signals from those areas with short spin-spin relaxation times die away before echo acquisition. The image in b) is "T_1 weighted." It has a short T_R (0.6 sec) and a short T_E (20 msec), and therefore is most sensitive to components, such as the water in fat, that have short relaxation times. The regions with long spin-lattice relaxation times remain saturated because of the rapid repetition rate and therefore have a reduced signal intensity.*

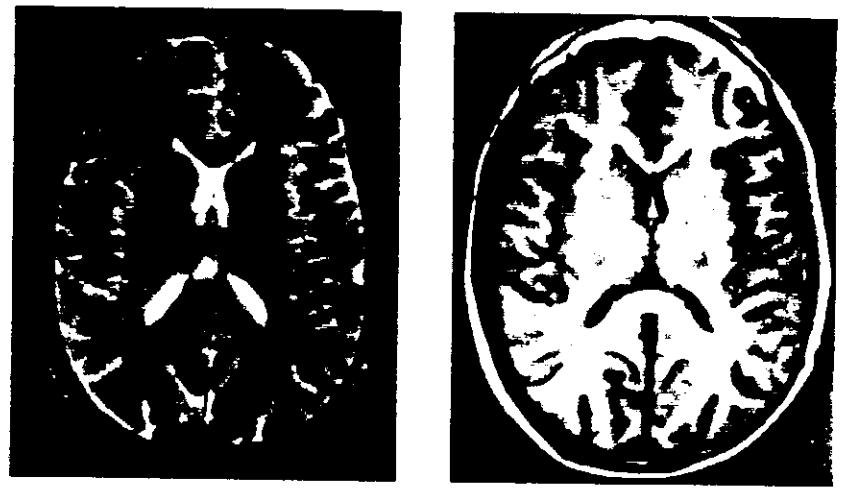

a b

NMR image obtained with the sequence of Figure 4 is given by:[17]

$$S = N_H[1 - 2e^{(-T_R - T_E/2)/T_1} + e^{-T_R/T_1}]\, e^{-T_E/T_2}$$

where N_H is the number of protons in the volume element, T_R is the repetition time between pulse sequences, and T_E is the echo time, which consists of the time between the 90° radiofrequency pulse and the formation of the spin echo. The effects of variations in T_R and T_E are illustrated by comparing two images taken of the identical slice of brain, but which differ in the relaxation weighting (*Figures 5a* and *b*). The bright parts of the image in Figure 5*a* show those parts of the brain, such as the ventricles, that have long spin-spin relaxation times (T_2s). Figure 5*b* highlights those parts of the brain that have short spin-lattice relaxation times (T_1s). Here the bone marrow is bright, whereas the ventricles, which have long T_1 relaxation times, are dark.

Examples

Although the medical applications are clearly responsible for the rapid growth of this technique, they are not the only uses for MRI. Selected examples are outlined, starting with several medical illustrations, and then describing several nonmedical uses.

Medical applications

Several examples of medical images came from a co-worker who has been having unexplained headaches. Among other tests, an MRI was recommended by his physician. *Figure 6a* shows an NMR image of a cross-section of his brain. This is one image of a series of nearly forty images that took a total of 30 min to acquire and cost $825. It is interesting to juxtapose this

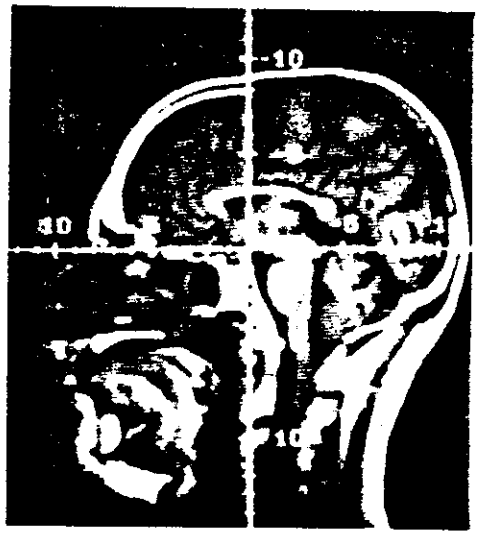

a

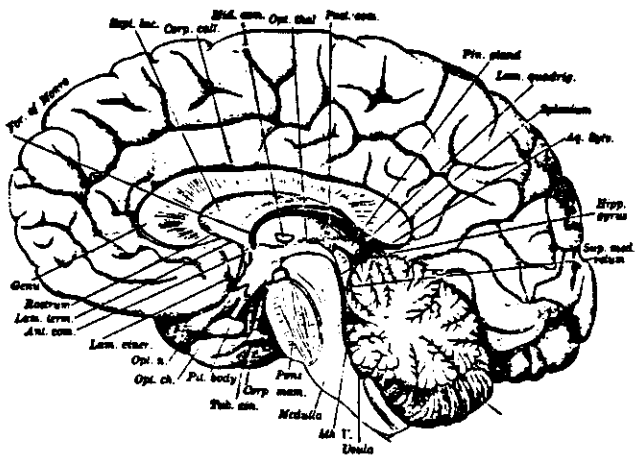

b

Figure 6 *a) An MRI juxtaposed with b), a figure taken from* Gray's Anatomy.[18] *Note that the white and grey matter in the brain is clearly distinguished, as are the corpus collosum, the cerebellum, the medulla, and sinus passages.*

image with a drawing taken from a copy of *Gray's Anatomy*[18] (1897) shown in Figure 6*b*. Although one cannot help but admire the beautiful drawings in this old anatomy book, recall that these drawings were necessarily made from cadavers.

In order to be imaged, the patient was asked to remove all metallic objects, such as his watch, and was slid into the bore of a magnet that is considerably larger than the research-sized system shown in *Figure 7*. He was fully awake during the imaging process and was asked to remain as motionless as possible. He felt no odd sensations, but was aware of the gentle knocking sound during image acquisition. The knocking sound arises from the mechanical disturbance of the gradient coils caused by the application of the large, switched magnetic field gradients.

In addition to providing invaluable information to neurologists, MRI is also being used to detect tumors, to image heart function, and to study blood flow. The wide extent of useful medical applications for MRI is only now beginning to be realized.

Blood flow and water transport

One promising application of NMR imaging is in the measurement of fluid flow. The basic idea is shown in *Figure 8*, where the slice selection pulse excites only those spins in the slice (Figure 8*a*). However, some fraction of these excited spins flow out of the slice by the time the signal is detected (Figure 8*b*). In their place in the slice are fresh spins, that is, spins that have not been excited by the 90° and 180° pulses.[19] Actual experiments are generally more complicated than the simple diagrams shown in Figures 8*a* and *b*. For blood flow, electrocardiographic gating of signal acquisition and signal subtraction techniques are used, together

Figure 7 *A 180-mm bore, 7.0 Tesla horizontal bore imager used for research purposes. Site preparation for horizontal magnets is generally expensive because they have large stray fields. The 5 Gauss line on this one, for example, extends out approximately 18 ft in either direction along the field axis. These systems must not be located near moving metallic objects such as elevators and trucks. One must also be careful when working around the magnet to keep metallic objects such as tools, laboratory equipment, and the computer and magnetic disk storage well away from the magnet. This particular magnet is mounted on a 6-ft tall platform to reduce stray fields in the room below the magnet and to increase the usable space in the vicinity of the magnet. The power supplies, radio frequency electronics, and computer are on the floor level and do not appear in the picture.*

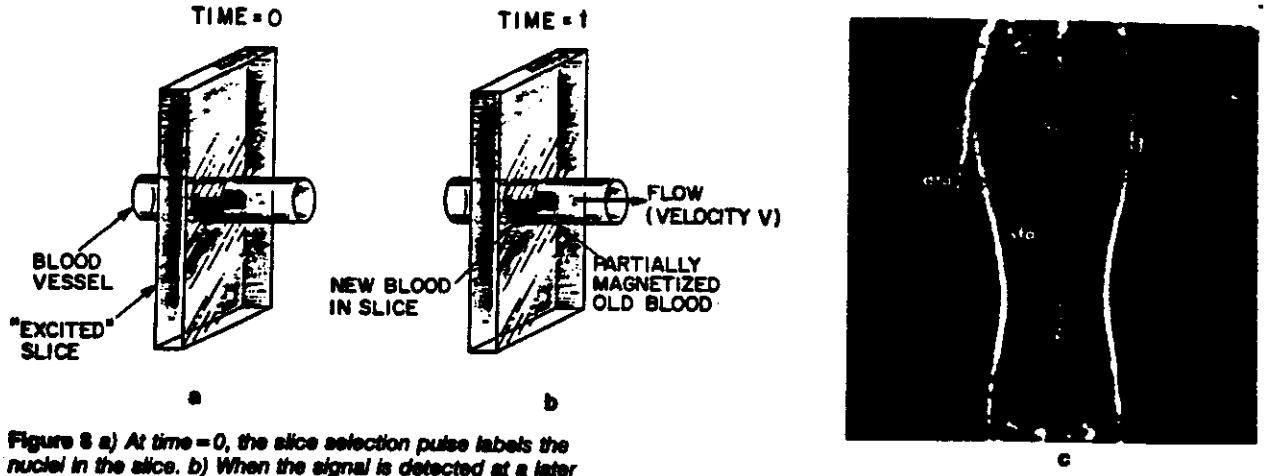

Figure 8 *a) At time = 0, the slice selection pulse labels the nuclei in the slice. b) When the signal is detected at a later time t, both the fresh and labeled blood are present in the imaging slice and will be detected. [(Adapted from F.W. Wehrli, J.R. MacFall, and T.H. Newton in "Advanced Imaging Techniques," T.H. Newton and D.G. Potts, Eds. (Clavadel Press, San Anselmo, California, 1983), p. 81]. c) Flow image of the thighs of a normal subject. sfa = superficial femoral artery; dfa = deep femoral artery. [(Reprinted from V.J. Wedeen et al., Science 230, 946 (1985) by permission of the American Association for the Advancement of Science.)]*

with velocity-dependent phase shifts. An application of this method is shown in Figure 8*c*, which shows a flow image of the thighs of a human.[20]

An alternative way to study flow and tissue perfusion is to perform deuterium NMR experiments, using the introduction of a bolus injection of D_2O.[21,22] The decay (washout) of the deuterium signal is then monitored and analyzed to obtain the rate of blood flow and perfusion of tissue.

Flow measurements are not limited to blood flow, and have been applied to the study of water transport in plant roots[23] and to the circulation of water within individual wheat grains.[24]

Nonbiological materials

Biological materials that contain large amounts of water (for example, the human body is approximately 80% water) have been discussed. Much of the water in biological systems is free, meaning that it is isotropically mobile on the NMR time scale ($\tau_c < 10^{-9}$ sec). Thus biological systems are ideal from a signal-to-noise standpoint, both because they have a high concentration of water and because this water has a narrow NMR linewidth.

The water or solvent taken up by nonbiological materials can also be imaged. For example, water interacts strongly with many polymers that have polar functional groups, most notably epoxy composites.[25] Since the water can plasticize the material and ultimately lead to component failure, the distribution of water uptake in polymer composites is of great interest. The water ingress into such systems has been imaged with much success,[26] as has the porosity in fired ceramic materials.[27] Magnetic resonance imaging can also be used to follow the time and spatial dependence of polymer curing or to measure the distribution of oil in a solid sample.[28]

All of these examples have involved NMR imaging of a component whose linewidth is narrow (water, oil, solvents). However, most materials (ceramics or polymers or fibers) do not have motionally narrowed lineshapes and cannot be imaged with standard imaging techniques. The exceptions are the elastomers such as polybutadiene, polydimethylsiloxane, and polyisoprene. One way to obtain images of these non-elastomeric materials is to use multiple-pulse methods and magic angle spinning techniques to narrow the proton lines, and to use rotating magnetic field gradients that are synchronized to the spinning of the sample.[29] Although the applicability of this method will probably be limited to samples that are small enough to spin (probably less than a gram or two), initial results show great promise in this technically difficult area.

Chemical shift imaging

Eventually researchers will want to image not only morphology, but also *function*,[30] as is currently done by positron emission tomography.[31] Here the goal is to obtain four-dimensional images; that is, stacks of two-dimensional slices where the fourth dimension is the chemical shift. Since the chemical shift contains information about the chemical identity and amounts of biological metabolites, volume-selective chemical shift imaging could provide an enormous amount of otherwise unavailable information. Although volume-localized chemical shift imaging has many signal-to-noise limitations,[32] it has been applied with success in several cases. These include observation of a locust egg during embryogenesis, where the ratio of the water to lipid was monitored from fertilization through to hatching.[33]

NMR microscopy

Nuclear magnetic resonance imaging at very high resolution is a current focus of much research interest. The ultimate resolution that will be achieved depends on the number of spins in the volume element, on the relaxation times of the water, on the sensitivity of the spectrometer, on the thickness of the slice, and on the strength of the magnetic field gradients. The maximum resolution that has been reported for a single cell (ova from *Xenopus*) is 10 μm × 13 μm pixels that are 250 μm thick.[34] The cytoplasm and defined regions of the nucleus could be visualized. This resolution is predicted to be close to the theoretical limit, since at this size the diffusion of water will be the limiting factor.[35] Water

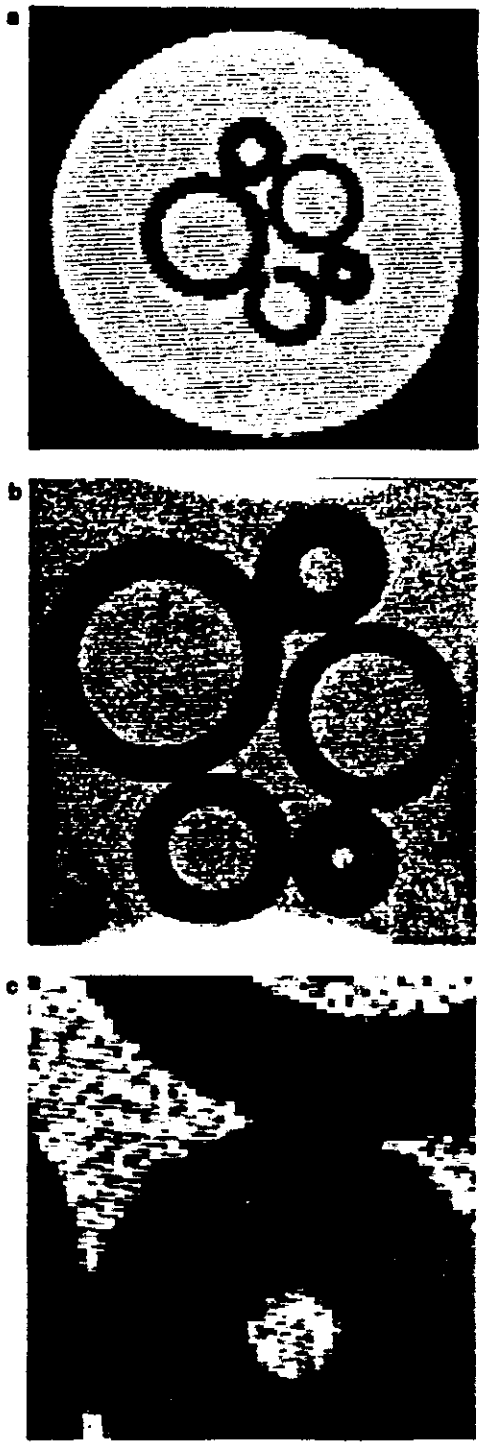

Figure 9 *a) Low resolution proton (8.4 Tesla) image of a phantom consisting of various saline (0.15 M NaCl) filled capillaries in a 10-mm tube which was also filled with the saline solution. The inner diameter of the smallest capillary is approximately 400 μm. b) Image with 20 μm × 20 μm × 800 μm resolution (before zero filling). c) An enlargement of the interior of the smallest capillary, where the pixel structure can be seen clearly.*

molecules could diffuse out of the pixel in the time required to obtain the echo. Others have shown that for biological tissue and 200-300 Hz linewidths, the relative intensity per pixel drops off steeply below 50 μm resolutions.[36] The decrease in signal intensity was more pronounced for water and gelatin (in which there could be free diffusion) than in liver and muscle, where the cell structure should limit the diffusion rate.

The following figures show some examples of microscopic imaging. *Figure 9* shows a phantom that was made by placing physiological saline (0.15 *M* NaCl) in various sized capillaries, and then placing these colinearly in a 10-mm tube which also contains the saline solution.[37] The inner diameter of the smallest capillary is 400 μm. Figure 9*a* shows an image of the entire phantom; Figure 9*b* shows the image when the resolution is increased to pixels that are 20 μm × 20 μm × 800 μm (before zero-filling). Note that signals outside the field of view in Figure 9*b* fold over into the image, causing potential confusion. Finally, the image in Figure 9*c* shows a close-up of the smallest capillary. Phantoms such as the one shown in Figure 9 present rather easy challenges. They don't move, they contain a lot of water, and they are generally constructed to have considerable symmetry in the plane of the slice.

Much more challenging is a live object, where one now has to contend with breathing artifacts, less signal, broader lines, and much less symmetry. An example of such an image is illustrated in *Figure 10*, which shows a cross-section of the neck of a rat.[38] This image was obtained with a surface coil in order to attain maximum sensitivity. The dark object in the left of the center in Figure 10*a* is the trachea. It is dark in this presentation because it is air-filled and therefore has no water signal. A water-filled capillary has been placed in the neck of the rat as a marker for the carotid artery. The carotid artery, to the right of the marker, appears dark because of flow effects. Figure 10*b* shows an image of a carotid artery obtained with 32 μm × 128 μm × 800 μm pixels (before zero filling). Even though signal folding occurs here also, the resolution and contrast are sufficient to locate the carotid artery and to quantify its size.

Future prospects for MRI

This article has illustrated applications of NMR imaging that range from whole bodies, to materials, to single cells. Current areas of intense interest and active research include measurement of flow, NMR microscopy, and chemical shift imaging. These fields are driven by the potential for an increased understanding of human disease and biological function. Because of its power for visualizing flow and heart beats, it is likely that MRI will enter into the domain of the cardiologist

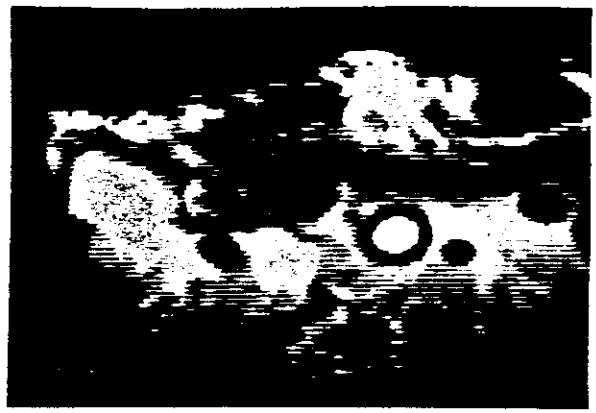

Figure 10 *a) Low resolution 8.4 Tesla proton image of the neck of an 80 g rat. The carotid artery and the jugular vein are visible to the right of the water-filled marker. b) Image obtained at 32 μm × 128 μm × 800 μm resolution (before zero filling) of the marker and the carotid artery.*

in the near future, as it is already in the domains of the neurologist and radiologist. The future will probably see non-invasive measurements of unprecedented resolution, as well as major advances in the imaging of biological function (i.e., four-dimensional imaging). These advances will undoubtedly be accompanied by strong progress in signal processing, instrumentation, data storage, and data retrieval methods, including optical disk storage, widespread high speed image transmission capabilities, and powerful three-dimensional reconstruction methods.

As in most fields, the future of a powerful and informative technique is limited only by the imagination, creativity, and innovation of scientists. The authors hope that this article has provided a glimpse of several promising applications, and that it has sparked the imaginations of the readers.

References

1. LAUTERBUR, P.C., *Nature (London) 242*, 190 (1973).
2. KLEINFIELD, S., *A Machine Called Indomitable* (Times Books, Div. of Random House, New York, NY, 1985).
3. "Commercializing High-Temperature Superconductivity," Congress of the United States, Office of Technology Assessment, p. 47, June 1988.
4. JELINSKI, L.W., *Chem. Eng. News 62*, 26 (1984).
5. BOVEY, F.A., *Nuclear Magnetic Resonance Spectroscopy*, 2nd ed., (Academic Press, New York, 1988).
6. DEROME, A.E., *Modern NMR Techniques for Chemistry Research* (Pergamon Press, New York, 1987).
7. SHOOLERY, J.N., *Am. Lab. 20* (10), 49 (1988).
8. MORRIS, P.G., *NMR Imaging in Medicine and Biology* (Clarendon Press, Oxford, 1986).
9. PYKETT, I.L., *Sci. Am. 246*, 78 (1982).
10. BOTTOMLEY, P.A., *Rev. Sci. Instr. 53*, 1319 (1982).
11. BUDINGER, T.F. and LAUTERBUR, P.C., *Science 226*, 288 (1984).
12. ERNST, R.R., *Quart. Rev. Biophys. 19*, 183 (1987).
13. SMITH, S.L., *Anal. Chem. 57*, 595A (1985).
14. ANDREW, E.R., *Proc. Royal Soc. Lond. B 225*, 399 (1985).
15. WARREN, W.S., *Science 242*, 878 (1988).
16. HINSHAW, W.S. and LENT, A.H., *Proc. of the IEEE 71*, 338 (1983).
17. MANSFIELD, P. and MORRIS, P.G., "NMR Imaging in Biomedicine" (Academic Press, New York, 1982).
18. GRAY, H., *Anatomy, Descriptive and Surgical*, (Lea Brothers & Co., New York, 1897) p. 756.
19. SINGER, J.R. and CROOKS, L.E., *Science 221*, 654 (1983).
20. WEDEEN, V.J. et al., *Science 230*, 946 (1985).
21. ACKERMAN, J.J.H. et al., *Proc. Nat'l. Acad. Sci. (USA) 84*, 4099 (1987).
22. KIM, S.G. and ACKERMAN, J.J.H., *Cancer Res. 48*, 3449 (1988).
23. BOTTOMLEY, P.A., ROGERS, H.H., and FOSTER, T.H., *Proc. Nat'l. Acad. Sci. (USA) 83*, 87 (1986).
24. (a) LAUTERBUR, P.C., *Nature 336*, 310 (1988). (b) JENNER, C.F., XIA, Y., BCCLES, C.D., and CALLAGHAN, P.T., *Nature 336*, 399 (1988).
25. JELINSKI, L.W. et al., *Macromolecules 18*, 1091 (1985).
26. ROTHWELL, W.P., HOLECEK, D.R., and KERSHAW, J.A., *J. Polym. Sci., Polym. Lett. Ed. 22*, 241 (1984).
27. ACKERMAN, J.L. et al., *Abstract for the 29th Experimental NMR Conference*, April 17-21, 1988, Rochester, New York, p. 53.
28. ROTHWELL, W.P. and VINEGAR, H.J., *Appl. Opt. 24*, 3969 (1985).
29. CORY, D.G., REICHWEIN, A., VAN OS, J.W.M., and VEEMAN, W.S., *Abstract for the 29th Experimental NMR Conference*, April 17-21, 1988, Rochester, New York, p. 50.
30. HOLDER, D.S., *Med. & Biol. Eng. & Comp. 2* (1) (1987).
31. DAGANI, R., *Chem. Eng. News 66*, 26 (1988).
32. ORDIDGE, R.J., CONNELLY, A., and LOHMAN, J.A.B., *J. Magn. Reson. 66*, 283 (1986).
33. LOHMAN, J.A.B. et al., *Abstract for the Society of Magnetic Resonance in Medicine, 5th Annual Meeting*, August 19-22, 1986, Montreal, Canada, p. 1119.
34. AGUAYO, J.B. et al., *Nature 322*, 190 (1986).
35. CALLAGHAN, P.T. and ECCLES, C.D., *J. Magn. Reson. 78*, 1 (1988).
36. MEYER, R.A. and BROWN, T.R., *J. Magn. Reson. 76*, 393 (1988).
37. BEHLING, R.W., TUBBS, H.K., and JELINSKI, L.W., unpublished data.
38. TUBBS, H.K. et al., unpublished data.

brief communication

Stroboscopic nuclear magnetic resonance microscopy of arterial blood flow

Ronald W. Behling, Helen K. Tubbs, Michael D. Cockman, and Lynn W. Jelinski
AT&T Bell Laboratories, Murray Hill, New Jersey 07974 USA

ABSTRACT NMR microscopy was used to obtain transverse flow profiles of arterial blood flow in the rat carotid artery at 33 μm resolution. The images were gated to the EKG and correspond to identified regions of diastole. The profiles show that flow is laminar during this part of the heart cycle. These results provide the first direct view of blood flow profiles in arteries of submillimeter diameter and suggest that animals as small as juvenile rodents will serve as valuable models for hemodynamic studies. Extensions to flow during systole, stenoses, and flow in the vicinity of the carotid bifurcation are discussed.

INTRODUCTION

Characterization of fluid flow is important in a wide variety of sciences, including analytical chromatography, reaction injection molding, botanical water transport, and medicine. Particularly in medicine, the visualization of blood flow is essential for characterizing normal and pathological states. In this report we show that stroboscopically sampled micromagnetic resonance imaging (micro-MRI) can be extended (Behling et al., 1989) to measure rapid arterial blood flow profiles in very small diameter 600–800 μm) arterial blood vessels in biologically accessible times. We furthermore show that flow is laminar at identified parts of the heart cycle. Considerations for obtaining optimum signal-to-noise under flow conditions are discussed and comparisons are made to gradient echo images.

Shortly after its discovery (Lauterbur, 1973), it was recognized that MRI could provide noninvasive information about fluid flow and about liquid diffusion. In the past decade a variety of schemes have been devised to measure flow. These include injecting a bolus of D_2O and performing deuterium NMR measurements (Ackerman et al., 1987; Kim and Ackerman, 1988), subtraction techniques that provide angiogram-like images of the cardiovascular system (Wedeen et al., 1985), phase images of slow venous blood flow (Pettigrew et al., 1987), influx of water into polymers and ceramics (Rothwell et al., 1984), and water diffusion and transport in plants (Jenner et al., 1988; Bottomley et al., 1986).

Spin-echo MRI can be used to measure flow in two different ways. The first involves time-of-flight considerations (Rittgers et al., 1988). Here, the flowing fluid, originally excited by the slice-selection pulse, either partially or completely flows out of the slice during the spin-echo time, leading to an intensity loss. This intensity loss is related to the flow rate, the echo time, T_E, and the slice thickness. The second basic method is based on the fact that the excited spins of a flowing fluid accumulate phase as they flow along a magnetic field gradient (Walker et al., 1988). The velocity is thus directly related to the phase angle. One can produce a phase-angle image where each pixel corresponds to the phase angle of the Fourier transform, given by the inverse tangent of the ratio of the imaginary and real data ($\tan^{-1}[I(f)/R(f)]$) (Brigham, 1974).

Although the phase angle image method is advantageous because only one image need be acquired, it suffers from signal-to-noise limitations when the flow is rapid. Rapid flow provides excellent contrast between flowing blood and the surrounding tissue because there is an *absence* of signal in the vessel, since the excited spins have flowed out of the slice before echo acquisition. However, the results presented here require the *presence* of a signal inside the artery. The experimental conditions used in this work (T_E = 20 ms, slice thickness = 800 μm), correspond to a flow rate cut-off of ~8 cm/s, above which flow cannot be observed. The flow during systole (approximately the first third of the heart cycle) in rats is too fast to be captured under these conditions; however, the flow at various points during diastole (the remaining two-

Dr. Behling's present address is Squibb Institute for Medical Research, Princeton, NJ 08543.

Dr. Tubbs's present address is Cornell Medical School, New York, NY 10021. Address correspondence to Dr. Jelinski, AT&T Bell Laboratories, 600 Mountain Ave., Murray Hill, NJ 07974.

0006-3495/90/07/267/05 $2.00

thirds of the heart cycle) is well within the window of observation.

MATERIALS AND METHODS

Approximately 80-g female Sprague-Dawley rats were anesthetized with ethyl carbamate (urethane, Sigma Chemical Co., St. Louis, MO) in 0.85% wt/vol saline using 850 mg/kg injected intraperitoneally, followed by 850 mg/kg injected subcutaneously behind the neck. The rats were intubated and a water-filled 10 mm × 1.35 mm (OD) capillary was inserted near the carotid artery as a marker for vertical positioning. Although after practice one can reliably position the rat in the probe and locate the carotid artery, the surgically implanted capillary is useful for obtaining unambiguous identification of the carotid artery when the field of view (FOV) is reduced. It is also useful as a control for the phase images *vide infra*. The incision was sutured and EKG leads were placed on the upper abdomen, well away from the surface coil, with the resultant electrocardiogram producing a V_3-like trace. The rat was placed head-down in a specially designed plastic rodent holder that was affixed to the probe. The temperature of the rats dropped to 31°C and stabilized there. They breathed an atmosphere of 60% oxygen and 40% nitrogen.

Either the *R* or the *S* wave of the EKG was used for gating. The output from the EKG was fed simultaneously to a frequency counter and to a model 485 oscilloscpe (Tektronix, Inc., Beaverton, OR). The "A gate" output from the oscilloscope was inverted and used to trigger the spectrometer. Because of the gating characteristics of the spectrometer and the oscilloscope, it was essential to use a short (microsecond) timebase on the oscilloscope. The spin-echo pulse sequence incoporated a time delay between the triggering and excitation. This delay was adjusted so that slice excitation corresponded to a known fraction of the heart cycle. The heart cycle was recorded periodically during each 13 min experiment and remained stable to within 3% during the 13-min experiment and ~10% during the typically 5 h required to acquire a series of data.

The NMR images were obtained using a spin-echo imaging sequence on a model AM 360 (Bruker Instruments, Inc., Billerica, MA) equipped with an NMR microscope accessory. The probe circuit was modified to accommodate a 1.4-cm-diameter, single-turn surface coil. A 2-ms lobeless sinc pulse was used for the slice-selective 90 and 180 Ċ pulses. The water linewidth was shimmed on the desired slice to ~100 hertz. The gradient strengths for the 33.9 × 33.9 × 0.8 mm FOV were 0.69, 0.74,

FIGURE 1 Gated transverse NMR image of the carotid artery of an 82-g rat. The field of view was 8.5 × 8.5 mm and the image corresponds to systole. The bright object is a saline-filled 10 × 1.35 mm (OD) glass capillary that was inserted near the carotid artery as a marker. The carotid artery is the ~800-μm dark object directly to the right of the marker. A smaller collateral artery (~50 μm) is also visible in this image. Parts of the trachea (*upper left*) and jugular vein (*upper right*) are also visible in this image.

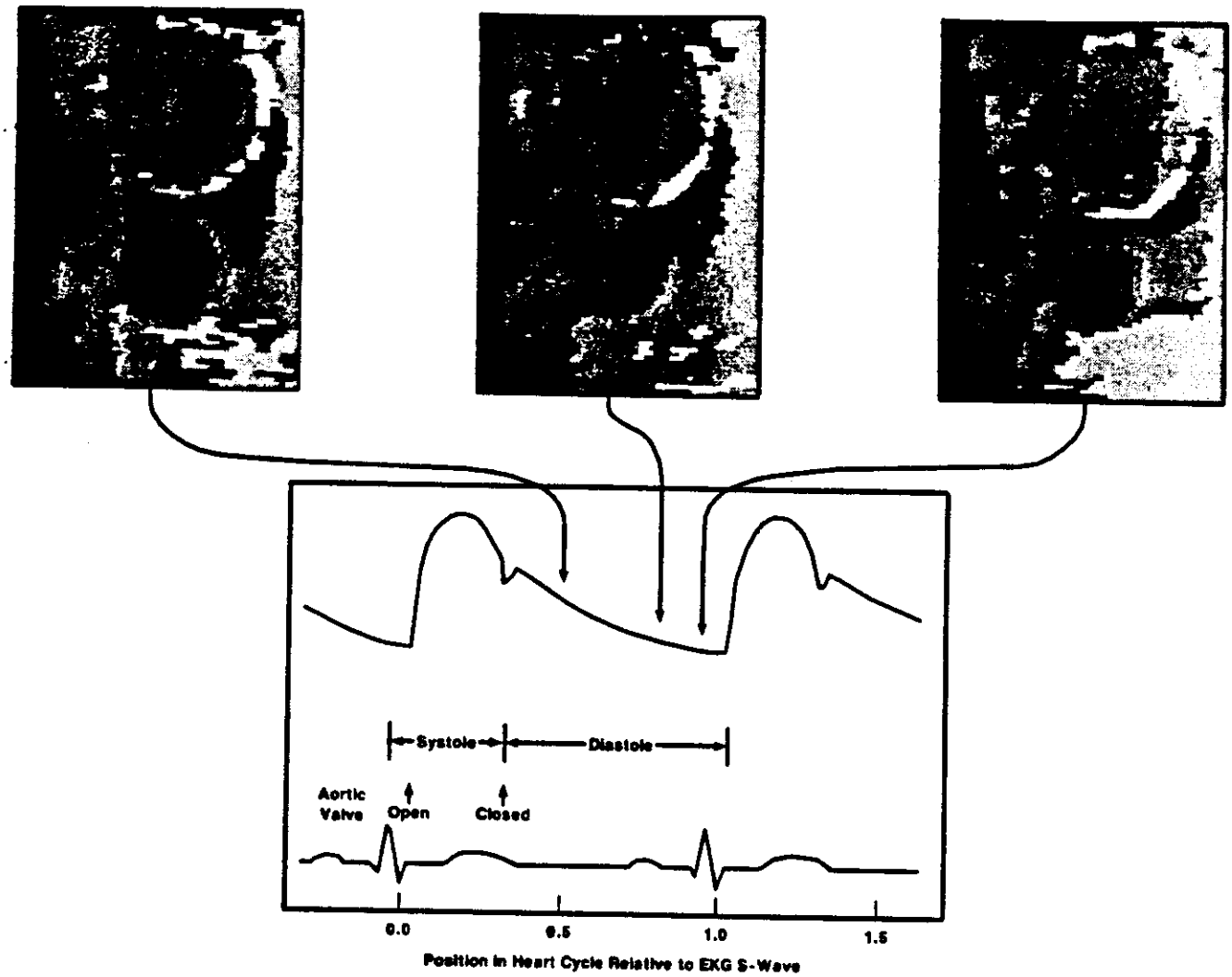

FIGURE 2 Phase images corresponding to various fractions (0.49, 0.77, and 0.91) of the heart cycle. The heart period was monitored three times during each image acquisition and was 158 ± 3 ms. The object at the top of the images is the water-filled marker. The liquid in the marker is not flowing and the liquid in the marker therefore reflects the level of noise and uncertainty of phasing in these images. The carotid, with its phase flow information, is the object directly below the marker. The gray scale corresponds to flow velocity.

and 1.8 Gauss/cm for the read-out (x), phase-encode (y), and slice-select (z) directions, respectively. For the 8.5 × 8.5 × 0.8 mm field of view the gradient strengths were 2.77, 1.48, and 1.8 Gauss/cm, respectively. The images consist of two scans of 256 points at each of 64 phase-encode increments surrounding the echo maximum. The repetition time (T_R) was 6 s. Although only 64 phase-encode increments were used, the size of the increment corresponded to the reduced FOV (i.e., whether using 256 or 64 phase encode gradients, the phase encode *increment* remained unchanged). 90° tip angles were used. The echo time (T_E) was set at 20 ms. The pixel size in the phase-encode direction was 132 and 33 μm in the read direction before zero filling. Slice thickness was ~800 μm.

Signal aliasing ("folding") in both dimensions must be tolerated to obtain images at the smaller field of view. Folding is less of a problem with a surface coil than with a volume coil because the signal from the surface coil drops off rapidly more than a radius distant from the coil. All images were carefully checked to ensure that folded-in signals did not affect the signals from the carotid artery or the marker.

The data were processed on a VAXStation II using version 4.9 of FTNMR from Dennis Hare. The data matrix was zero filled to 512 × 512 before Fourier transformation; no signal enhancement or digital filtering was applied to the data. Because we collected echoes that were not centered within the acquisition window, large first-order phase corrections were required. The phase image was constructed by taking the inverse tangent of the angle between the imaginary and real data for each voxel. Velocities were determined using the equation:

$$v_z = 0.048\phi_z,$$

where v_z is the velocity along the z-direction in cm/s and ϕ_z is the phase

angle in degrees. This method of determining flow velocities was verified using a calibrated flow phantom.

RESULTS AND DISCUSSION

Fig. 1 shows a typical micro-MRI image of the carotid artery, gated so the image corresponds to the peak of systole. The bright object surrounded by the dark rim is the 1.35-mm OD saline-filled glass marker. The fully-expanded carotid artery is immediately to the right of the marker, and a smaller collateral artery appears on the right side of the carotid. A portion of the trachea is also visible on the upper left of Fig. 1, and part of the jugular vein appears on the upper right. Data of the high resolution shown in Fig. 1 require that extreme attention be paid to all details of the imaging experiment. This includes signal-to-noise considerations and shimming on the slice that will be examined. The gating must be reliable and the echo time as short as possible. Breathing artifacts were not a problem because the rat was sufficiently immobilized. The artery appears dark in this image because it corresponds to the extreme peak of systole, where essentially all of the originally excited blood had flowed out of the artery before the echo was acquired.

We have previously shown that we can map the dimensional changes of the carotid artery over the entire heart cycle and have furthermore demonstrated a noninvasive method for measuring Young's modulus of the artery from the NMR data (Behling et al., 1989). Having demonstrated the ability to obtain images that correspond to clearly identified parts of the heart cycle, we now obtain and analyze images to obtain noninvasive profiles of blood flow. Examples of such images are shown in Fig. 2, where three phase-images are displayed above an idealized blood pressure waveform. The outline of the water-filled marker appears at the top of each of these images. Because there is no flow in the liquid in the marker, there should be no phase variation across the marker. The small amount of phase variation that is observed reflects sources of phase such as magnetic field and RF inhomogeneity. The carotid is the dark object directly below the marker, where the effects of flow are observed directly. Here the gray scale corresponds to flow velocity. (Explicit flow velocities are summarized below.)

The data of Fig. 2 can be plotted in perspective form rather than with gray scales; these are shown in Fig 3. The three perspectives correspond directly to the carotid artery region of the data shown in Fig. 2; the vertical axis corresponds to the flow velocity. These data appear to map out a parabolic flow profile. Investigation of slices taken from Fig. 3 show that the flow is fairly symmetrically disposed about the artery. Cross-sections at the position of maximum flow (approximately at the midpoint of the artery) are shown in Fig. 4 (*solid lines*). The sloping baseline, seen in Fig. 2, was assumed to arise from sources of phase other than flow and was subtracted for this figure. These data have been fit to a parabola (*dotted lines*) showing that the flow is indeed laminar. The maximum flow velocities at 0.49, 0.77, and 0.91 of the heart cycle are 7.5, 6.0, and 4.0 cm/s, respectively.

These experiments are not without difficulties and further technical advances must be attained for a more complete realization of the initial work presented here. For example, the T_E in the spin-echo sequence imposes a finite cut-off time, and the T_E of 20 ms used in these experiments is too long to capture the rapid blood flow during systole. Using a variety of techniques, including actively shielded gradients, one could perhaps reduce the

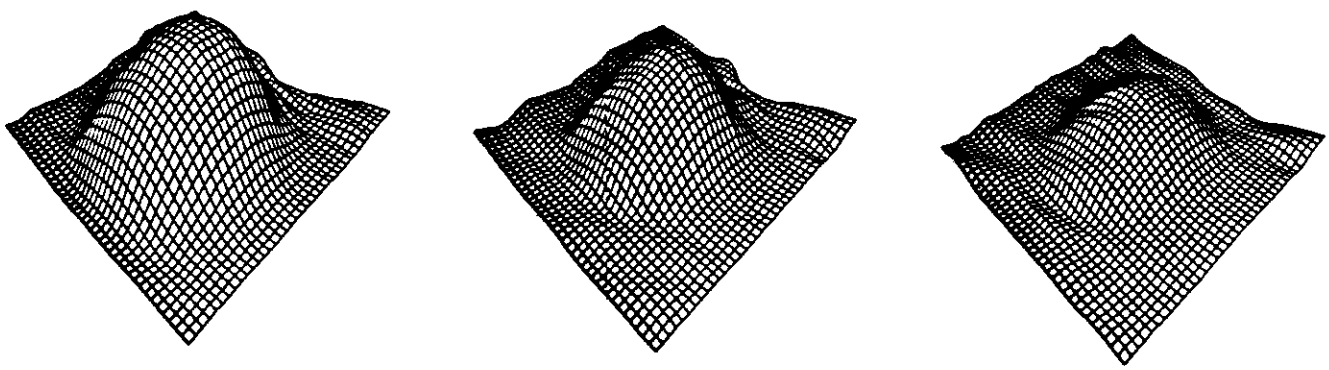

FIGURE 3 Perspective drawings of the blood flow data presented in Fig. 2. The vertical axis corresponds to velocity; the velocity scale is shown explicitly in Fig. 4.

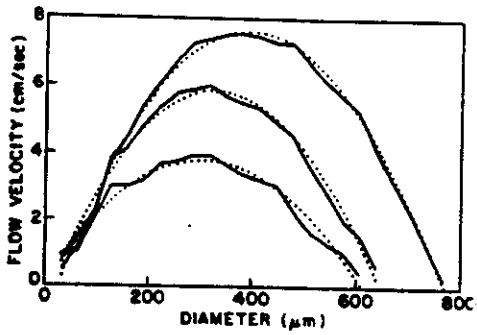

FIGURE 4 Blood flow velocity as a function of position across the carotid artery. The three solid lines correspond to the data of Fig. 3 after the sloping baseline was subtracted out. These represent data from fractional positions in the heart cycle of 0.49, 0.77, and 0.91. The dotted lines are a fit to a parabola ($y = ax^2 + b$).

T_E to at least half its present value. We have investigated the alternative approach of using a gradient echo instead of the spin-echo sequence used in this work. Although one can capture images throughout the entire heart cycle, we find that the gradient echo under flow conditions is especially sensitive to the effects of magnetic field inhomogeneities and that the images are difficult to phase.

These results provide the first direct view of blood flow profiles in arteries of submillimeter diameter. They demonstrate that stroboscopically sampled MRI can provide direct and detailed information about blood flow patterns. The blood flow pattern in the carotid artery was laminar throughout diastole. These results are significant for several reasons. First, they demonstrate that animals as small as juvenile rats are suitable as models for hemodynamic investigations. The ability to use rodents for such studies reduces the cost and complexity of performing experiments on blood flow. Furthermore, these experiments provide the groundwork for important extensions investigating blood flow in the presence of stenoses, near occlusions, and in the vicinity of the carotid bifurcation.

Received for publication 6 October 1989 and in final form 13 March 1990.

REFERENCES

Ackerman J. J. H., C. S. Ewy, N. N. Becker, and R. A. Shalwitz. 1987. Deuterium nuclear magnetic resonance measurements of blood flow and tissue perfusion employing ^2H_2O as a freely diffusible tracer. *Proc. Natl. Acad. Sci. USA.* 84:4099–4102.

Behling R. W., H. K. Tubbs, M. D. Cockman, and L. W. Jelinski. 1989. Stroboscopic NMR microscopy of the carotid artery. *Nature (Lond.).* 340:321–322.

Bottomley, P. A., H. H. Rogers, and T. H. Foster. 1986. NMR imaging shows water distribution and transport in plant root systems in situ. *Proc. Natl. Acad. Sci. USA* 83:87–89.

Brigham, E. O. 1974. The Fast Fourier Transform. Prentice-Hall, Inc., Englewood Cliffs, NJ. 12.

Jenner, C.F., Y. Xia, C. D. Eccles, and P. T. Callaghan. 1988. Circulation of water within wheat grain revealed by nuclear magnetic resonance micro-imaging. *Nature (Lond.).* 336:399–402.

Kim, S.-G., and J. J. H. Ackerman. 1988. Multicompartment analysis of blood flow and tissue perfusion employing D_2O as a freely diffusible tracer: a novel deuterium NMR technique demonstrated via application with murine RIF-1 tumors. *Magn. Res. Med.* 8:410–426.

Lauterbur, P. C. 1973. Image formation by induced local interactions: examples employing nuclear magnetic resonance. *Nature (Lond.).* 242:190–191.

Pettigrew, R. I., W. Dannels, J. R. Galloway, T. Pearson, W. Millikan, J. M. Henderson, J. Peterson, and M. E. Bernardino. 1987. Quantitative phase-flow MR imaging in dogs by using standard sequences. *Am. J. Roentgeneol.* 148:411–414.

Rittgers, S. E., D.-y. Fei, K. A. Kraft, P. P. Fatouros, and P. R. S. Kishore. 1988. Velocity profiles in stenosed tube models using magnetic resonance imaging. *Trans. ASME (Am. Soc. Mech. Eng.) J. Biomech. Eng.* 110:180–184.

Rothwell, W. P., D. R. Holecek, and J. A. Kershaw. 1984. NMR imaging. Study of fluid absorption by polymer composites. *J. Polym. Sci. Polym. Lett. Ed.* 22:241–247.

Walker, M. F., S. P. Souza, and C. L. Dumoulin. 1988. Quantitative flow measurement in phase contrast MR angiography. *J. Comp. Assisted Tomogr.* 12:304–313.

Wedeen, V. J., R. A. Meuli, R. R. Edelman, S. C. Geller, L. R. Frank, T. J. Brady, and B. R. Rosen. 1985. Projective imaging of pulsatile flow with magnetic resonance. *Science (Wash. DC).* 230:946–948.

Reprinted from Nature, Vol. 341, No. 6240, pp. 321-323, 28th September, 1989

Stroboscopic NMR microscopy of the carotid artery

Ronald W. Behling*, Helen K. Tubbs*, Michael D. Cockman & Lynn W. Jelinski†

AT&T Bell Laboratories, Murray Hill, New Jersey 07974, USA
* Present addresses: Squibb Institute for Medical Research, Princeton, New Jersey, NJ 08543, USA (R.W.B.) and Cornell Medical School, New York, 10021 USA (H.K.T.)
† To whom correspondence should be addressed

THE non-invasive measurement of vascular dynamics and elasticity is critical in understanding haemodynamic conditions of cardiovascular diseases such as hypertension and atherosclerosis[1]. Although there are numerous invasive and *in vitro* techniques[2] for such measurements, until now non-invasive methods have been limited[3]. We have now obtained stroboscopic NMR images[4,5] of the carotid arteries of 80-g rats. The change in the cross-sectional area of arteries of diameter ~600–800 μm was correlated with the change in absolute blood pressure. These are the first microimages[6–9] of a dynamic system and enable the direct visualization of compliance, the non-invasive measurement of Young's modulus, the direct determination of the local effects of vasoconstrictors and vasodilators and the mapping of the entire cardiac cycle.

Figure 1 (left panel) shows a large-field-of-view (FOV) spin-echo NMR image of the left side of the neck of an 80-g rat, whereas the images shown in the middle and right panels correspond to systole and diastole, respectively. The carotid artery at systole appears dark (corresponding to the absence of signal) because the blood that was excited during slice selection had flowed out of the slice by the time the echo was obtained. Fresh unexcited blood had taken its place, thereby affording great contrast. The image at diastole is an extreme example of a complete loss of contrast that occurs when the blood flow is so slow that it is difficult to distinguish between the blood in the artery and the water in the surrounding tissue. This effect was observed only rarely (more representative images at diastole are shown in Fig. 3), and the echo time (T_E) could be adjusted to change the intensity of the blood signal in the artery.

Data such as these shown in Fig. 1 were analysed by drawing expanded plots, the contours of which correspond to the grey levels in the image. Representative plots are shown in Fig. 2. Each of the areas of these plots was measured independently by three individuals, using a planimer. The averages of the three normalized measurements for two rats are shown in Fig. 3. The error bars correspond to the standard error of the three separate measurements. The error is small near systole (~2%) and larger near diastole (~8%) because of the flow effects mentioned above.

The cross-sectional areas of the carotid artery at the extremes of systole and diastole can be correlated with the absolute blood pressure to determine the distensibility, related to the compliance, of the carotid artery. Compliance is defined as the volume change per unit of pressure; our measurements, however, recorded a change in the cross-sectional area. We have assumed that the length of the carotid artery did not change appreciably during the heart cycle, an assumption that is valid in view of separate measurements of the transverse and longitudinal Young's modulus (see below). The distensibility is calculated by:

$$\frac{(A_{\text{systole}} - A_{\text{diastole}})/A_{\text{diastole}}}{P_{\text{systole}} - P_{\text{diastole}}} \times 100\%$$

where P_{systole} and P_{diastole} are the absolute blood pressures at systole and diastole, respectively, and A_{systole} and A_{diastole} are the corresponding arterial cross-sectional areas. The average distensibility was determined as 1.1% per mm Hg (range 0.67–1.36%) from the NMR data for six rats.

These NMR data provided a unique opportunity to measure non-invasively the transverse Young's modulus of the carotid artery. The Young's modulus E is a measure of the elasticity of a material and increases as the material stiffens. It is defined by E = stress/strain, or

$$E = \frac{2\pi r_0}{s} k$$

(ref. 10) where r_0 is the artery radius at zero pressure and s is the corresponding thickness of the arterial wall. For a section of artery of length l, the constant k is related to the force tangental to the arterial wall F and to the pressure P exerted by the blood on the arterial wall by

$$F = Prl = kl[2\pi(r - r_0)]$$

where r is the arterial radius at pressure P. From this expression,

$$\Delta P = 2\pi k \Delta r / r$$

Integration gives

$$(P_{\text{systole}} - P_{\text{diastole}}) = 2\pi k[\ln(r_{\text{systole}}/r_{\text{diastole}})],$$

where r_{systole} and r_{diastole} are the arterial radii at systole and diastole, respectively. Thus, we could determine k from the

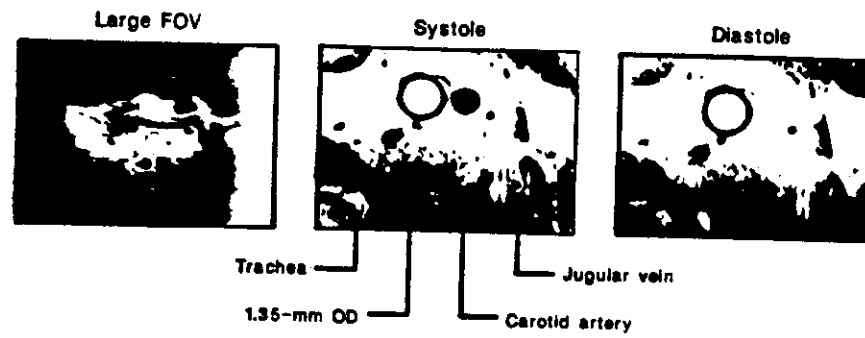

FIG. 1 Spin-echo NMR images of the left side of the neck of an 80-g rat. Left, Field of view (FOV) 33.9 × 33.9 mm; middle, FOV 8.5 × 8.5 mm; this image corresponds to systole. Right, FOV 8.5 × 8.5 mm; image corresponds to diastole.
METHODS. Female Sprague-Dawley rats (80 g) were anaesthetized with ethyl carbamate (urethane, Sigma) in 0.85% saline (w/v) by injecting 850 mg of the solution per kg (body weight) intraperitoneally, and then injecting 850 mg per kg subcutaneously behind the neck. The rats were intubated and a water-filled capillary (10 mm × 1.35 mm o.d.) was inserted near the carotid artery as a marker for vertical positioning. The incision was sutured and electrocardiograph leads were placed on the upper abdomen, away from the surface coil, with the resultant electrocardiogram producing a V_3-like trace. The rat was placed head-down in a specially designed plastic rodent holder that was affixed to the probe. The temperature of the rats decreased to 31 °C and stabilized at that level. They breathed 60% O_2 and 40% N_2. The NMR images were obtained using a Bruker AM 360 equipped with an NMR microscope accessory. The probe circuit was modified to accommodate a 1.4-cm-diameter single-turn surface coil. A 2-ms lobeless sinc pulse was used for the slice-selective 90°-and 180° pulses. The water line-width was shimmed on the desired slice to ~100 Hz. The gradient strengths for the 33.9 × 33.9 × 0.8-mm FOV were 0.69, 0.74 and 1.8 gauss cm^{-1} for the read-out (x), phase encode (y) and slice select (z) directions, respectively. For the 8.5 × 8.5 × 0.8-mm FOV the gradient strengths were 2.77, 1.48 and 1.8 gauss cm^{-1}, respectively. The images consisted of two scans at each of 64 phase-encode increments surrounding the echo maximum. The pixel size in the phase-encode direction was 132 μm, and 33 μm in the read direction before zero filling. The data matrix was zero filled to 512 × 512 before Fourier transformation; no signal enhancement or digital filtering was applied to the data. Slice thickness was ~800 μm. The repetition time (T_R) was 6 s and the echo time (T_E) was 20 ms.

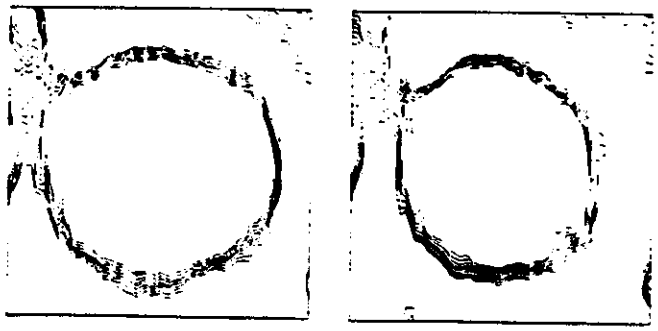

FIG. 2 Representative contour plots for cross-sectional area determinations.

available NMR data and once k was obtained, calculate r_0 by setting $P_{diastole}$ to zero. The thickness of the artery at zero pressure must be known. We measured the average thickness of an excised artery from an 80-g rat using a light microscope as 0.10 ± 0.02 mm.

The average Young's modulus was calculated as 7×10^5 dyn cm^{-2} for six rats (range 4.9×10^5-1.3×10^6 dyn cm^{-2}). This can be compared with a value of 6.5×10^5 dyn cm^{-2} for the transverse modulus of an excised carotid from an 80-g rat, measured mechanically with a Rheovibron viscoelastometer. (The longitudinal Young's modulus was 3.1×10^6 dyn cm^{-2}.) The agreement between the NMR measurement of Young's modulus and the classical Rheovibron measurement is remarkable, considering the errors associated with keeping the sample moist during the viscoelastic measurements, and the assumption that the arterial thickness is identical for all arteries.

The NMR method can also be used to provide non-invasive information about the local action of vasoactive drugs. The vasoconstrictor phenylephrine affects primarily the small arterioles. As the heart beats more slowly, this results in a compensatory increase in the cardiac output. The carotid artery, therefore, must expand to accommodate this increase in volume—such an expansion may be observed directly (data not shown). Figure 4 shows the cross-sectional areas of the carotid arteries of five rats, normalized to the pre-drug systole area, plotted against the blood pressure, with and without phenylephrine. The linearity of the data shows that the drug raised the blood pressure without affecting the distensibility of the carotid artery. Similar experiments were performed with the vasodilator nitroprusside. Although the variation between rats was greater

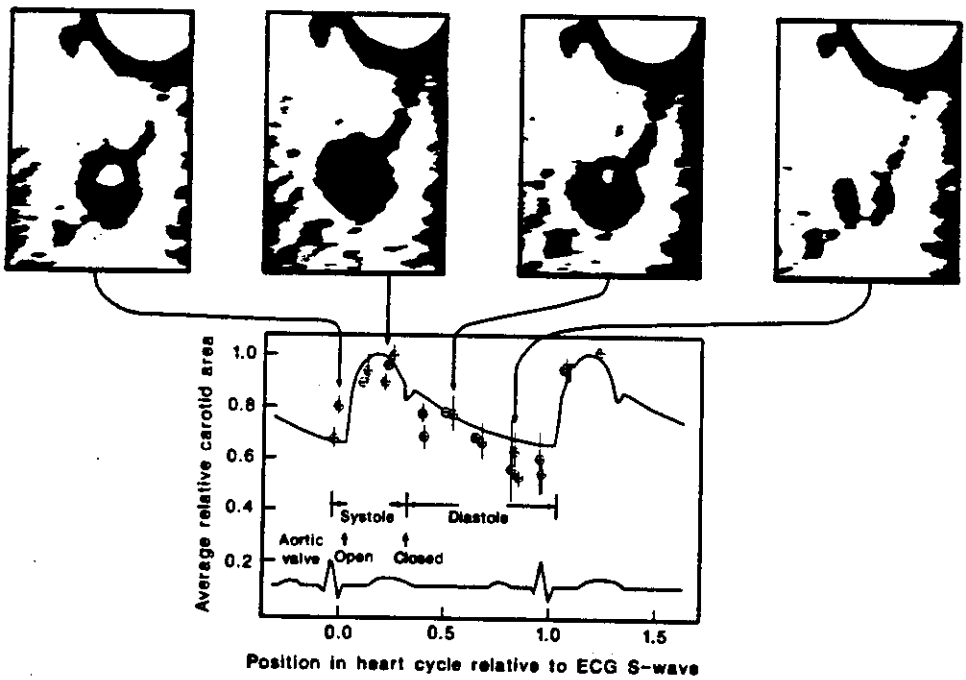

FIG. 3 Arterial cross-sectional area as a function of phase in the heart cycle. The line through the data corresponds to blood pressure in a human heart cycle and is intended only as a guide to the eye.
METHODS. Either the R- or the S wave of the electrocardiogram was used for gating. The spin-echo pulse sequence incorporated a time delay between the triggering and excitation. This delay was adjusted so that slice excitation corresponded to a known fraction of the heart cycle. The heart period (typically 150 ms) was recorded periodically and remained stable to within 3% during the 13-min experiment and ~10% during the 5 h typically required to acqure a series of data.

FIG. 4 Plot of the normalized cross-sectional area of the carotid artery versus blood pressure for five rats, with and without phenyleph ine. The data before and after administration of the vasoconstrictor were fully reversible. ○, Control, systole; ●, control, diastole; +, drug dose 1, systole; ×, drug dose 1, diastole; □, drug dose 2, systole; ■, drug dose 2, diastole; ◇, post-drug systole; ◆, post-drug diastole.
METHODS. Blood pressure was measured using a catheter inserted into the right carotid artery. A 1.5-cm length of polyethylene tubing (0.61 mm OD, 0.28 mm ID, Clay Adams PE 10) was inserted into the artery; it was joined to a 2.9-m length of larger (0.965 mm OD, 0.58 mm ID, Clay Adams PE 50) polyethylene tubing, filled with a solution of normal saline with heparin (10 USP units ml^{-1} saline), that led out of the magnet to the pressure transducer (Spectramed P23XL). The artery was periodically flushed with heparinized saline (0.1 ml) The blood pressure typically remained stable to ~5% systole and ~8% diastole during ~5 h total experimental time. The right jugular vein of the rat was catheterized with a 2.9-m length of polyethylene tubing (PE 10). This led to a calibrated syringe pump (Sage Instruments, model 355). For an 80-g rat, phenylephrine (Sigma; 1 mg ml^{-1} in normal saline) was delivered at ~7.5 μl min^{-1}, with small variations needed to keep the blood pressure constant. For an 80-g rat, sodium nitroprusside (0.08 mg μl^{-1}; Sigma) in 5% dextrose (w/v) was delivered at 13 μl min^{-1}.

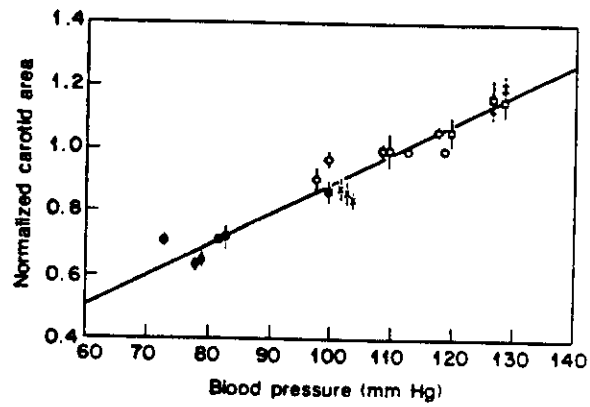

in these experiments, the data suggest that the dilation of the artery at diastole with the drug was greater than that without it.

The data shown here were obtained for the carotid artery of 80-g rats, whose arteries were ~600–800 μm in diameter. We predict that it is possible to observe changes under high-contrast conditions when there are 4–5 pixels across the artery. This would set a lower limit of 2.5–3 mm for the diameter of human vessels that can be measured accurately, given the 0.5-mm resolution so far available on whole-body machines. □

Received 31 May; accepted 15 August 1989.

1. Yamakoshi, K.-I. & Kamiya, A. *Med. Prog. Through Technol.* **12**, 123–143 (1987).
2. Hayashida, N., Okui, K. & Fukuda, Y. *Jap. J. Physiol.* **37**, 183–196 (1987).
3. Dahn, I., Jonson, B. & Nilsén, R. *J. appl. Physiol.* **28**, 328–332 (1970).
4. Hinshaw, W. S. & Lent, A. H. *Proc. IEEE* **71**, 338–350 (1983).
5. Ernst, R. R. *Q. Rev. Biophys.* **18**, 183–220 (1987).
6. Johnson, G. A. *Bull. Am. phys. Soc.* **34**, 445 (1989).
7. Aguayo, J. B., Blackband, S. J., Schoeniger, J., Mattingly, M. A. & Hintermann, M. *Nature* **322**, 190–191 (1986).
8. Cho, Z. H. *et al. Med. Phys.* **15**, 815–824 (1988).
9. Callaghan, P. T. & Eccles, C. D. *J. magn. Reson.* **78**, 1–8 (1988).
10. Elias, H.-G. *Macromolecules: Structure and Properties* 2nd edn. 425 (Plenum, New York, 1984).

ACKNOWLEDGEMENTS. We are grateful to Alan Tubbs, Seiji Ogawa, Chester Gieniewski and Lee Blyler for helpful discussions.